Brillouin Light Scattering Studies of Topological Insulators Bi_2Se_3, Sb_2Te_3, and Bi_2Te_3

by

Jamal Najr Alnofiay

A thesis submitted
in partial fulfillment of the
requirements for the degree of
Master of Science

Department of Physics and Physical Oceanography
Memorial University of Newfoundland
October 2014

St John's Newfoundland & Labrador

Abstract

Brillouin Light Scattering has been used to examine acoustic waves in three different Topological Insulators: Bismuth Selenide Bi_2Se_3, Antimony Telluride Sb_2Te_3, and Bismuth Telluride Bi_2Te_3. Two samples of each material were studied to ensure the accuracy of the results obtained. In general, surface mode, quasi-transverse, and quasi-longitudinal bulk modes were observed in all these materials. Rayleigh surface phonon velocities were obtained for the first time from the corresponding Brillouin peak frequency shifts. Quasi-transverse and quasi-longitudinal bulk mode velocities were also obtained. Elastic constants C_{33} and C_{44} were calculated from the measured bulk-velocties. Both bulk acoustic phonon velocities and elastic constants were compared to those obtained in previous studies. All results obtained have been found to be in good agreement with both experimental and some theoretical available studies.

Acknowledgments

First and foremost, I would like to express my sincere gratitude to my supervisor, Dr. Andrews for continuous support of my master's study and research, for his patience, motivation, enthusiasm, and immense knowledge. His guidance helped me in all the time of research and writing of this thesis. I could not have imagined having a better supervisor for my master's study.

I would like to thank all my family members for supporting me and being the biggest part of this success. Special thanks and sincere appreciation to my parents for being patient waiting for me while I am abroad. They are the only reason behind everything good I have ever made.

It is my sincere pleasure to express my great appreciation to Dr. Alothaib for all of his assistance. I will be forever indebted for him for his help and insightful guidance during my being in St. John's.

Finally, huge thanks to the Ministry of Higher Education in the Kingdom of Saudi Arabia for the scholarship I have been granted.

Contents

List of Tables

List of Figures

Chapter 1

Introduction

1.1 Topological Insulators Overview

Topological insulators (TIs) are a new class of materials that have just been known due to the unique properties they possess, and they have therefore been intensively examined both theoretically and experimentally [1, 2, 3]. TIs combine two of the classifications of condensed matter materials: conductor and insulator. The surfaces of TIs are conductive and contain mobile electrons while these materials are insulating in the bulk even though it is a single material [4, 5]. This means that an energy gap exists in the bulk of a topological insulator while its surfaces or edges do not contain an energy gap. Because of the interactions that emerge in such materials between the valance states and the conduction states, some states in the valence band exchange positions with some states in the conduction band through the edges of the material. This leads electrons to move freely and make such materials conductor only on surfaces. The states, a valence state and a conduction state, join electrons in pairs where one spin up and the other is down. The interesting part is that electrons of such materials are restricted to move in a certain direction with a specific spin. They

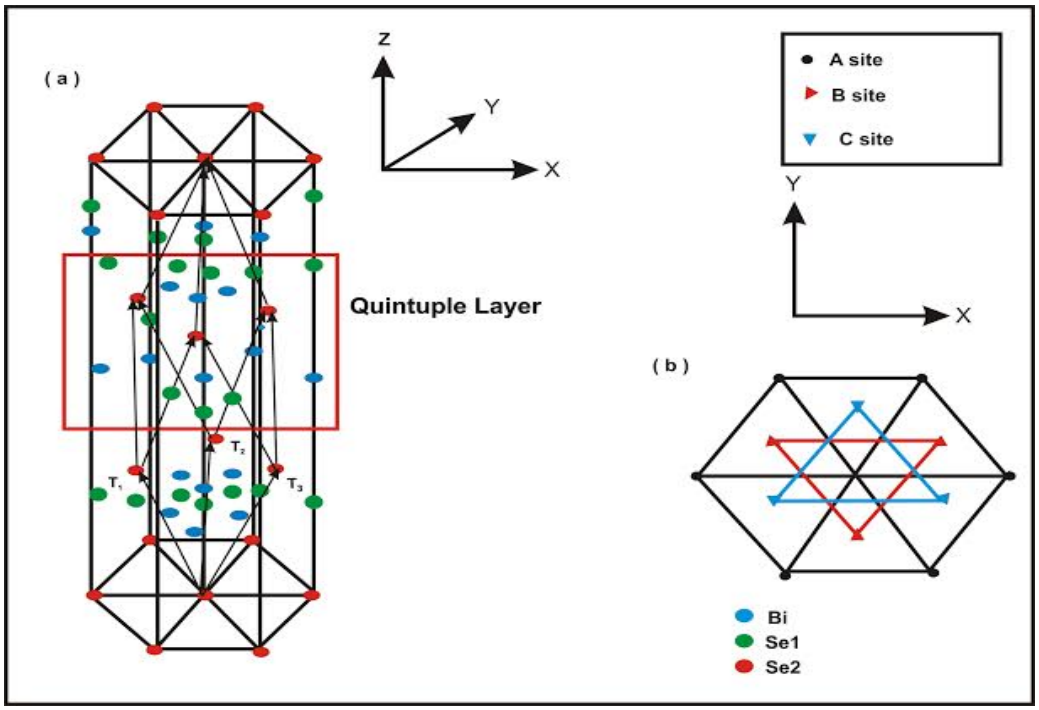

Figure 1.1: Lattice structure of the topological insulator Bi_2Se_3. (a) hexagonal structure consisting of 15 layers, and the primitive cell containing five atoms placed in three positions. (b) top view of Bi_2Se_3 indicating three possible positions for atoms.

cannot change direction nor spin which makes the current on the surface hard to be deformed. It has been noticed that insulators have a weak current on the surface, but it is very easy to be deformed unlike topological insulators which are topologically protected [4]. This feature makes these materials useful and will bring a big enhancement in the scientific environment. This is because the current will remain unchanged when the material is deformed, corrupted, or contaminated due to the topological protection. Recently, because of the unusual structure and the strange behaviour of such materials, a great amount of attention has been paid in condensed matter physics to study and analyze them [6, 7].

Bi_2Se_3, Sb_2Te_3, and Bi_2Te_3 are a family of Topological Insulators. They exhibit a bulk band gap due to spin-orbit coupling where the surface consists of metallic states due to the topological protection. These materials have a rhombohedral lattice symmetry layered structure with space group D_{3d}^5 ($R\bar{3}m$). The layered structure has five atomic layers constructing the unit cell, they are called quintuple layers as can be seen in the red box in Figure 1.1, and every single layer constitutes a triangle lattice [8]. The Van der Waals bonding between layers is weak; however, since the bonding within one layer is covalent, it is much stronger than the bonding between layers [9]. A unit cell is shown in Figure 1.1.(a) containing 5 atoms with the translation vectors $\vec{t}_1$, $\vec{t}_2$, and $\vec{t}_3$. It is also shown that one of the Se atoms is placed at (0 0 0), two atoms of Bi are placed at (±M ±M ±M) from the origin, and the two other atoms of Se are placed at (±N ±N ±N), where M and N are the distance from the origin. By looking at the top of the compound, there are three possibilities for atoms to be placed in the layer: site A, site B, and site C as shown in Figure 1.1 (b).

1.2 Previous Studies of Elastic Properties of Bismuth and Antimony Chalcogenides

Much attention has been paid to the investigation of the optical, structural, and electronic properties of Bi_2Se_3, Sb_2Te_3, and Bi_2Te_3. However, only a little emphasis has been placed on characterizing the elastic properties of such materials, and no one has reported results of Brillouin scattering experiments on these materials.

Theoretical studies of elastic properties has mostly focused on the use of first-principles calculations using the density functional theory within the local density

approximation. Koc *et al.* [10] calculated the elastic constants of Sb_2Te_3, and Bi_2Te_3 utilizing the first principles calculations. They also calculated related parameters such as Young's modulus, shear modulus, and bulk modulus. Longitudinal and transverse waves velocities of Sb_2Te_3, and Bi_2Te_3 were also calculated in order to calculate the Debye temperature by averaging the sound velocities [10]. Xiong *et al.* [11] determined the elastic constants for four different structural phases (I, II, III, IV) of Bi_2Te_3 at 0 pressure; using the same method. The elastic constants were calculated in order to predict the mechanical stability, brittle character, and elastic anisotropy. For the structural phase I, which has trigonal symmetry, six independent elastic constants were determined. For other structural phases, which are monoclinic, 13 independent elastic constants were determined. Young's modulus, shear modulus, and bulk modulus were also calculated. The results obtained in this work were found to be in good agreement with experimental data [12]. Moreover, first-principles calculations along with the quasi-harmonic Debye model were used by Feng *et al.* [13] to determine the elastic constants and bulk modulus of Bi_2Te_3 at 0 K and 0 pressure.

Tong *et al.* [14] used the interaction potentials to investigate structural, mechanical, and elastic properties of Bi_2Te_3 at different temperatures. In their study, they found that all elastic constants decrease linearly with increasing temperature. The results of elastic constants presented in this work are smaller than the values which are experimentally obtained [12]. They referred to the fact they considered pure crystals in their simulation, while in experiments impurities exist which may account for the observed difference.

The elastic constants as well as Young's modulus and shear modulus of Bi_2Te_3 were determined at different temperatures by Huang *et al.* [15]. They applied a combination of Boltzmann transport equations, first-principles calculations, and molecular dynamics simulations. The energy surface of Bi_2Te_3 was scanned by varying the

bond lengths. The classical potentials with predetermined forms were fitted to this data via the GULP code. The elastic properties were then studied by implementing the potentials in the GULP package. Good agreement was found with the available experimental data [12].

Koc *et al.* [16] computed the elastic constants of Bi_2Se_3 using the volume-conserving technique and the strain-stress relationship for SIESTA and VASP calculations, respectively. According to [16], there are neither theoretical nor experimental results for Bi_2Se_3 in order to compare and verify the results they obtained.

The longitudinal and transverse acoustic phonon velocities of Bi_2Te_3 were estimated by Yang *et al.* [17] in studies of the thermal conductivity of this material. In their study, both in-plane and cross-plane thermal conductivities were calculated using frequency-dependent solutions of the Boltzmann transport equation, and combined by means of the rule of the analytical averaging. The phonon dispersion relation was estimated using the Born-von Karman Einstein model. Consequently, the longitudinal and transverse phonon velocities were found which makes the model used in this study (BvKE) more accurate than the Debye approximation due to the reasonable analysis of the group velocity.

Jacquot *et al.* [18] presented a model of the anisotropy of the lattice thermal conductivity of a single of Bi_2Te_3. This model discusses the acoustic phonon in terms of cutoff frequencies. Longitudinal and transverse acoustic phonon velocities, in the basal plane of the unit cell and perpendicular to it, have been estimated from plots and tabulated in Table 4.9.

Jenkins and Rayne [12] experimentally determined the elastic constants of Bi_2Te_3 at different temperatures ranging from 0 K to 300 K in order to observe the effect of the temperature on the elastic constants using a continuous-wave resonance technique. The values obtained in this work correspond to a limiting Debye temperature of 164.9

± 0.2 K, and they were found to be in an excellent agreement with the calorimetric value of 165 ± 0.2 K.

The ultrasonic pulse-echo technique was used by Akgoz *et al.* [19] in order to obtain the six independent elastic constants of $Bi_{1.60}Sb_{0.40}Te_3$ at 300 and 77 K. They compared their results to another experimental result of Bi_2Te_3 [12] to study the effect of substituting of antimony atoms for bismuth. It was found that both materials show high acoustic velocities in the xy plane, and much lower velocities along the direction z where the interatomic binding is weak. Even though the weakest binding in Bi_2Te_3 is between tightly bound sets of five layers, while in $Bi_{1.60}Sb_{0.40}Te_3$ is between pairs of layers, they exhibit a similar elastic behaviour. In addition, longitudinal and transverse acoustic phonon velocities were calculated in different directions of propagation and temperatures.

1.3 Motivation

As is clear from the previous section, some theoretical work has been done on elastic properties of the bismuth and antimony chalcognides [10-11, 13-16], but experimental work is quite limited [12, 19]. Furthermore, there have been few theoretical works that report the acoustic phonon velocities in Bi_2Se_3, Sb_2Te_3, and Bi_2Te_3 [10, 17-19], and no experimental results have been reported. In particular, there have been no reports of surface phonon velocities. Knowledge of acoustic phonon velocities could lead to the determination of the elastic constants of these materials. In addition, while there are a good number of studies on the elastic properties of Bi_2Te_3, the reported works of elastic constants of Bi_2Se_3 and Sb_2Te_3 are theoretical and quite limited in number.

In this work, the technique of Brillouin light scattering is used for the first time to probe the elastic properties of the bismuth and antimony chalcogenides, Bi_2Se_3, Sb_2Te_3, and Bi_2Te_3. Both surface and bulk acoustic phonon velocities have been determined for Bi_2Se_3, Sb_2Te_3, and Bi_2Te_3. Some elastic constants have also been estimated. When possible, comparison is made to results obtained in previously published work. In particular, the results obtained for Bi_2Se_3 and Sb_2Te_3 can then be used for the comparison with the theoretical results obtained by others techniques, such as first principle calculations, in order to figure out how accurate the models used for such calculations. Also, Bi_2Te_3 results can be compared to experimental data and the results of theoretical studies where an inconsistency in the values of elastic constants obtained in different studies has been observed [10-13, 15]. From a technological standpoint, detailed information on the elastic properties of bismuth and antimony chalcogenides is important if these materials are to be used in practical applications such as acousto-optic devices. From a fundamental perspective, accurate knowledge of the elastic properties can serve as a reference point for the testing of

theoretical models that attempt to predict the mechanical properties of this family of topological insulators.

Chapter 2

Theory

2.1 Elasticity

2.1.1 Definition

Applying a force on an object causes a deformation either in the shape or the volume due to the displacement occurred for atoms in the object. A material is described to be elastic when it returns to its original volume and shape after removing an applied force. What distinguishes a material from being elastic or inelastic is the answer to the question: Did it return to its original shape or not? In fact, no material is perfectly elastic, and a deformation should occur when a force is applied. This leads one to think about the elastic limit which means the limit of elasticity that an object can be elastically deformed where Hooke's law is valid below this limit. This means that, the relation between the stress and strain is linear, and the object will be distorted by exceeding this limit of elasticity [20].

2.1.2 Theory of Elasticity

Acoustic phonons have long wavelengths in comparison to primitive cell dimensions. This means that they act like sound waves in a continuous medium, and the discreteness of the crystal is neglected due to the long wavelengths. Therefore, the equations of motion of these waves can be written as [21]

$$\rho \frac{d^2 u_i}{dt^2} = C_{ijkl} \frac{d^2 u_i}{dx_j dx_k}, \tag{2.1}$$

where ρ is the mass density of the material, $\frac{d^2 u_i}{dt^2}$ is the acceleration in the $i-th$ direction, u_i is the particle displacement along the $i-th$ direction, and C_{ijkl} is the fourth rank elastic constants tensor.

Noting that when the medium is slightly deformed, the stress T_{ij} is proportional to the strain S_{kl} as expressed in Hooke's law

$$T_{ij} = C_{ijkl} S_{kl} \tag{2.2}$$

Because the stress and the strain tensors are symmetric, S_{kl}=S_{lk} and T_{ij}=T_{ji}, leading to C_{ijkl}=C_{jilk}=C_{jlkl}=C_{ijlk} which makes the number of independent elastic constants 36 instead of 81. It is convention to use Voigt notations to reduce the number of subscripts of the elastic constants from 4 to 2 as follows [22]:

(11)$\longleftrightarrow$(1) , (22)$\longleftrightarrow$(2)

(33)$\longleftrightarrow$(3) , (23) = (32)$\longleftrightarrow$(4)

(31) = (13)$\longleftrightarrow$(5) , (12) = (21)$\longleftrightarrow$(6)

As a result, the elastic constants tensor may be written in the following form:

$$\begin{bmatrix} C_{11} & C_{12} & C_{13} & C_{14} & C_{15} & C_{16} \\ C_{12} & C_{22} & C_{23} & C_{24} & C_{25} & C_{26} \\ C_{13} & C_{23} & C_{33} & C_{34} & C_{35} & C_{36} \\ C_{14} & C_{24} & C_{34} & C_{44} & C_{45} & C_{46} \\ C_{15} & C_{25} & C_{35} & C_{45} & C_{55} & C_{56} \\ C_{16} & C_{26} & C_{36} & C_{46} & C_{56} & C_{66} \end{bmatrix} \tag{2.3}$$

Hooke's law therefore can be written as $T_\alpha = C_{\alpha\beta} S_\beta$. Since the lattice symmetry of the topological insulators Bi_2Se_3, Sb_2Te_3, and Bi_2Te_3 is rhombohedral, the number of independent elastic constants may be reduced to six and the elastic constants tensor then takes the form [23, 24]:

$$\begin{bmatrix} C_{11} & C_{12} & C_{13} & C_{14} & 0 & 0 \\ C_{12} & C_{11} & C_{13} & -C_{14} & 0 & 0 \\ C_{13} & C_{13} & C_{33} & 0 & 0 & 0 \\ C_{14} & -C_{14} & 0 & C_{44} & 0 & 0 \\ 0 & 0 & 0 & 0 & C_{44} & C_{14} \\ 0 & 0 & 0 & 0 & C_{14} & \frac{1}{2}(C_{11} - C_{12}) \end{bmatrix} \tag{2.4}$$

For the determination of the equation of motion in a material, Newton's second law is linked to Hooke's law as stated in Equation 2.1 where Newton's second law is [21]

$$\rho \frac{d^2 u_i}{dt^2} = \frac{dT_{ij}}{dx_j}, \tag{2.5}$$

For plane waves, the particle displacement in the $i-th$ direction is

$$\vec{u}_i = u_i^o e^{i(\vec{k}.\vec{r}-wt)} \tag{2.6}$$

where u_i^o is the polarization of the wave.

Now, substituting Equation 2.6 into Equation 2.1 gives the Christoffel equation

$$\rho v^2 \delta_{ij} - C_{ijkl} n_j n_k = 0, \tag{2.7}$$

where $\hat{n}$ is the unit vector pointing in the direction of propagation, v is the phonon velocity, and δ_{ij} is the Kronecker delta. Defining $\Gamma_{ij} = C_{ijkl} n_j n_k$, the Christoffel equation can be written as :

$$\Gamma_{ij} - \rho v^2 \delta_{ij} = 0 \tag{2.8}$$

The velocities of the acoustic waves are then obtained by solving the secular equation:

$$|\Gamma_{ij} - \rho v^2 \delta_{ij}| = 0 \tag{2.9}$$

The eigenvalues provide ρv^2 for three different modes, two of them are quasi-transverse and one is quasi-longitudinal, while the eigenvectors give the polarization vectors for each eigenvalue ρv^2.

Along the z-axis of a rhombohedral crystal, C_{33} and C_{44} can be calculated from these expressions [25]

$$v_L = \sqrt{\frac{C_{33}}{\rho}} \tag{2.10}$$

$$v_T = \sqrt{\frac{C_{44}}{\rho}} \tag{2.11}$$

where v_L (v_T) is the quasi-longitudinal (quasi-transverse) phonon velocity.

2.2 Brillouin Light Scattering

Brillouin Light Scattering Spectroscopy is the technique employed in this work to determine acoustic phonon velocities and elastic properties of topological insulators Bi_2Se_3, Sb_2Te_3, and Bi_2Te_3. This technique has gained substantial interest since its invention by Leon Brillouin in 1922. The theoretical proposal of Brillouin spectroscopy by L. Brillouin was experimentally proven by Gross [26]. This invention was not initially considered as a great advancement since a monochromatic light source was not available, which made obtaining useful information from Brillouin spectroscopy difficult. This issue was resolved with the invention of the laser in the 1950s. Since then, Brillouin Spectroscopy has been widely used as an effective tool for analyzing the scattered light from various media [27, 28, 29, 30].

In order to differentiate the types of scattering in all media, it is very important to have a background about how the scattering process works. The process of scattering is defined as the deviation of the incident photons from their straight propagation due to collisions with particles in a medium such as phonons. There are two different types of scattering: elastic and inelastic scattering. An example of elastic scattering is Rayleigh scattering, in which energy and momentum of an incident photon remain unchanged. However, when a change in energy and momentum occurs, the process is called inelastic scattering. Raman and Brillouin scattering are well known examples

of such scattering.

In a solid, acoustic phonons and optical phonons are the two different types of vibrations of atoms since the atoms vibrate about their equilibrium positions because of the thermal energy. An optical phonon is generated when atoms are vibrating in opposite directions resulting in higher energy; this type of phonon is probed in Raman scattering experiments which typically employ grating spectrometers to analyze the scattered light [31, 32]. However, when atoms are oscillating in phase (i.e. moving together in the same direction), the interaction energy is lower, and this type of vibration is called an acoustic phonon. Acoustic phonons cause the Brillouin scattering of the incident photons and require that a Fabry-Perot interferometer be used as the spectrometer due to the low frequencies involved. The process of Brillouin scattering involves the interaction between the incident electromagnetic waves and the material, causing a change in the energy and momentum of the incident waves [33]. The energy and momentum will be exchanged between the incident photon and the material, giving the scattered photon different values of energy and momentum from the incident photon [34, 35]. In Brillouin scattering, the change in energy can be seen as an increase when a phonon is annihilated, or as a decrease when the phonon is created [36]. It is clearly shown in Figure 2.1 that the inelastic scattering encompasses two significant phenomena, phonon emission and phonon annihilation. The former phenomenon is often termed as Stokes scattering whereas the latter is usually called anti-Stokes scattering [37]. These two phenomena can be symbolically distinguished by signs as shown in Equations (2.12) and (2.13). The negative sign represents the Stokes component where some energy is lost in order to create the phonon. In contrast, the positive sign refers to the anti-Stokes component where some energy is gained from annihilating a phonon [7, 38]. Figure 2.2 illustrates schematically the energy difference between Stokes and anti-Stokes and compares them to Rayleigh

scattering, where no loss or gain in incident light energy occurs.

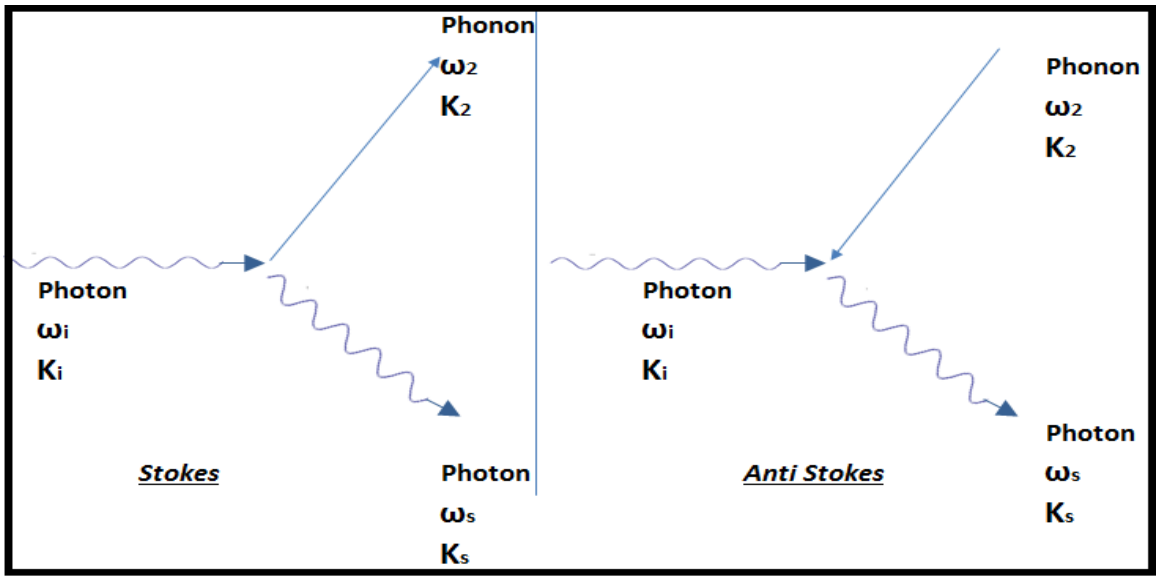

Figure 2.1: Phonon creation and phonon annihilation representing Stokes and anti-Stokes scattering, respectively. ω_i (k_i) are the frequency (wavevector) of the incident photon, ω_2 (k_2) are the frequency (wavevector) of created or annihilated phonon, ω_s, (k_s) are the frequency (wavevector) of the scattered photon, respectively.

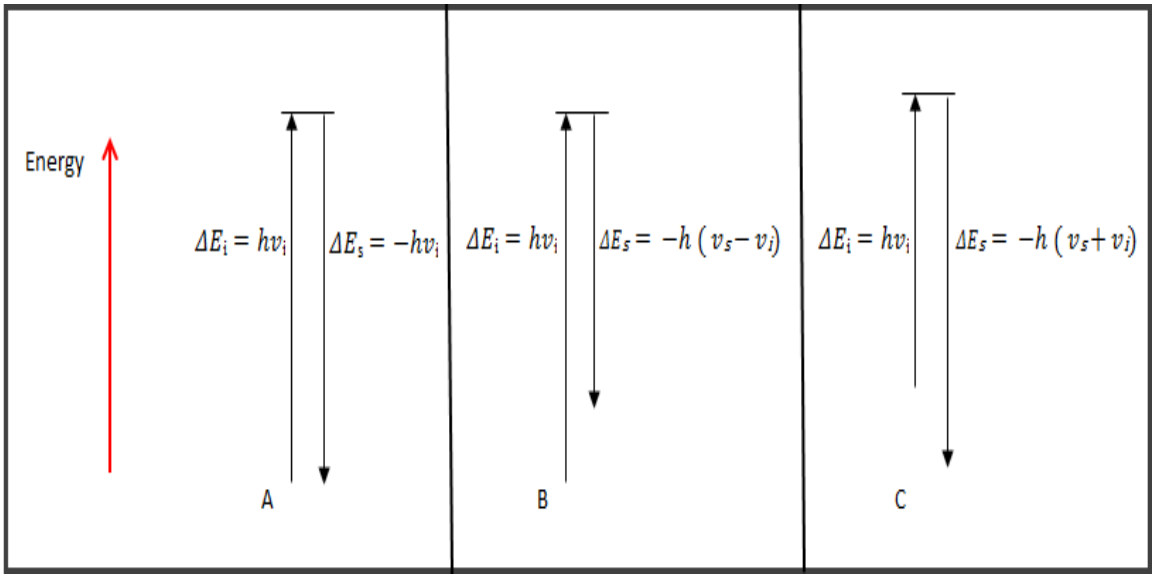

Figure 2.2: Comparison between (A) Rayleigh scattering where the energy of incident photons is unchanged, (B) Stokes scattering where some energy of incident photons is lost , and (C) anti-Stokes scattering where the energy of incident photons is increased.

The conservation of momentum and energy relations for the scattering process may be written as [39]

$$\hbar\vec{k_i} = \hbar\vec{k_s} \pm \hbar\vec{k}' \tag{2.12}$$

$$\hbar\omega_i = \hbar\omega_s \pm \hbar\omega' \tag{2.13}$$

where $\hbar$ is Planck's constant, $\vec{k}'$, $\vec{k_i}$, and $\vec{k_s}$ are the wavevectors of the phonon, incident photon, and scattered photons, respectively, as shown in Figure 2.3, and ω', ω_i, and ω_s are the corresponding angular frequencies [39]. It can be noted from Equation (2.13) that the frequency of the phonon is equal to the difference between the incident and scattered light frequencies.

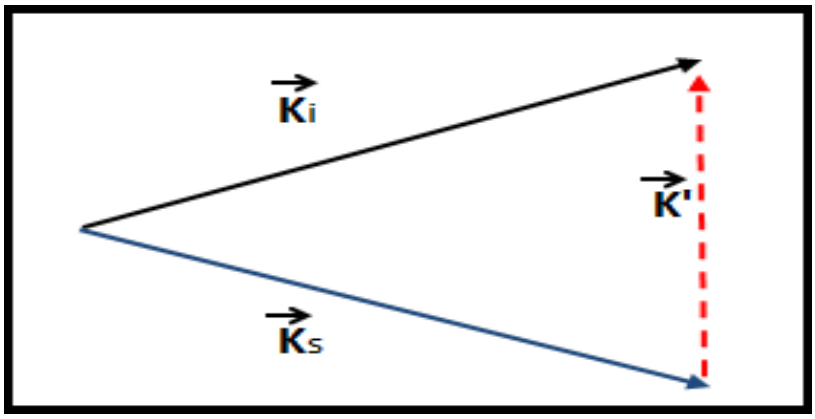

Figure 2.3: Relationship between incident light wavevector, scattered light wavevector, and phonon wavevector in the scattering process.

2.3 Scattering from Acoustic Waves

Acoustic waves in a solid being studied in this work can be either Rayleigh surface phonons or bulk phonons. The peak due to Rayleigh surface phonon (labelled R in Figure 2.4) has a lower frequency shift in the Brillouin spectrum than those for the bulk phonons [35]. The phonons that travel inside the material are quasi-transverse bulk modes (particle displacement predominantly in a direction perpendicular to the direction of propagation, (labelled (T_1) and (T_2) in Figure 2.4), and quasi-longitudinal bulk modes (particle displacement predominantly parallel to the direction of propagation, (labelled L in Figure 2.4).

2.3.1 Scattering from Rayleigh Surface Modes

One of the waves that propagates on the surface of a material is the Rayleigh surface mode which has primarily transverse character. Brillouin spectroscopy has been used extensively to study surface phonons because this technique can provide accurate measurement of their velocities.

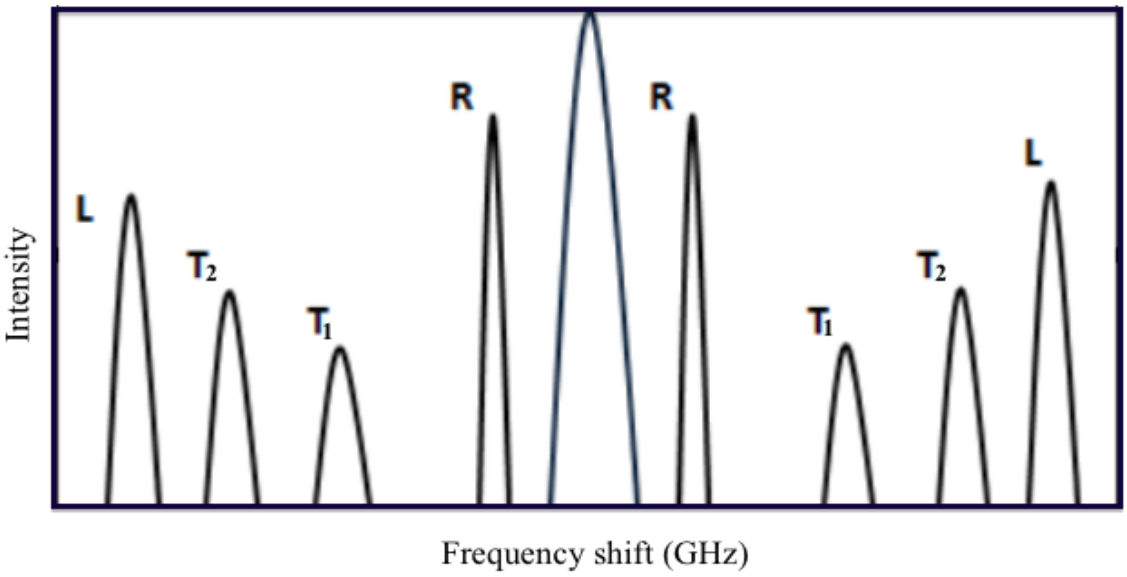

Figure 2.4: Schematic Brillouin spectrum showing peaks due to Rayleigh surface mode (R), slow quasi-transverse (T_1), fast quasi-transverse (T_2), and quasi-longitudinal bulk modes (L).

As can be seen in Figure 2.5 and by applying principle of conservation of momentum to the scattering process (2.12), the following expression can be obtained

$$k'_{s\parallel} = k_i \sin\theta_i + k_s \sin\theta_s \tag{2.14}$$

$$k'_{s\perp} = n(k_i \cos\theta_i + k_s \cos\theta_s) \tag{2.15}$$

where $k_{s\parallel}$ and $k_{s\perp}$ are the parallel and the perpendicular components of the scattered photon wave vector, respectively. $k'_{s\parallel}$ and $k'_{s\perp}$ are the parallel and perpendicular components of the surface phonon wave vector. It is noteworthy to mention that the perpendicular component of the surface phonon to the surface can be neglected. The reason for this is that the amplitude of the surface phonon rapidly vanishes with distance from the surface. Thus Equation 2.15 breaks down and then k'=$k'_{s\parallel}$.

$$k' = k_i \sin\theta_i \pm k_s \sin\theta_s \tag{2.16}$$

where θ_i (θ_s) is the angle between the incident (scattered) photon and the surface normal. It is noticeable that the angular frequency of incident light is much larger than the angular frequency of phonon. Thus, as shown in Figure 2.3 [40]

$$k_i \approx k_s. \tag{2.17}$$

Additionally, by considering that the geometry used in the present work is backscattering, we have $\theta_i = \theta_s$ as shown in Figure 2.5. Equation 2.16 may be then written as

$$k'_s = 2k_i \sin\theta_i \tag{2.18}$$

where k'_s is the magnitude of the wave vector of the surface phonon. Knowing that k_i=$2\pi/\lambda$ and substituting this into Equation 2.18, one obtains:

$$k'_s = \frac{4\pi}{\lambda} \sin\theta_i \tag{2.19}$$

where λ is the wavelength of the incident light. For long wavelength acoustic phonons [9],

$$\omega' = v_s k'_s \tag{2.20}$$

where ω', v_s and k'_s are the angular frequency, velocity, and magnitude of the surface phonon wavevector, respectively. From Equations 2.19 and 2.20, it is possible to write, for the case of backscattering such as used in this work, the Brillouin frequency

shift, $f=\frac{\omega'}{2\pi}$ [41], for the Rayleigh surface mode as

$$f = \frac{2v_s}{\lambda}\sin\theta_i. \tag{2.21}$$

This allows the Rayleigh surface phonon velocity to be measured from the associated Brillouin peak frequency peak shift. It may also be noted that the Brillouin frequency shift of the Rayleigh surface phonon peak depends on the angle of incidence θ_i.

2.3.2 Scattering from Bulk Modes

As can be seen in Figure 2.5 and by applying principle of conservation of momentum to the scattering process (2.12), the following expressions can be obtained for the parallel $k'_{b\parallel}$ and perpendicular $k'_{b\perp}$ components of the bulk phonon wavevector

$$k'_{b\parallel} = k_i\sin\theta_i + k_s\sin\theta_s \tag{2.22}$$

$$k'_{b\perp} = n(k_i\cos\theta'_i + k_s\cos\theta'_s). \tag{2.23}$$

The magnitude of the bulk mode wavevector can be written as

$$k'_b = \sqrt{{k'_{b\parallel}}^2 + {k'_{b\perp}}^2} \tag{2.24}$$

where

$$k'^2_{b\parallel} = k_i^2\sin^2\theta_i + k_s^2\sin^2\theta_s + 2k_ik_s\sin\theta_i\sin\theta_s \tag{2.25}$$

$$k'^2_{b\perp} = n^2k_i^2\cos^2\theta'_i + n^2k_s^2\cos^2\theta'_s + 2n^2k_ik_s\cos\theta'_i\cos\theta'_s. \tag{2.26}$$

Therefore, Equation 2.24 can be written as the following where $k_i = k_s$, $\sin\theta_i = n\ \sin\theta_i'$ and $\theta_i = \theta_s$ for backscattering geometry

$$k_b' = [4n^2k_i^2(\sin^2\theta_i' + \cos^2\theta_i')]^{1/2} \tag{2.27}$$

As a result

$$k_b' = 2nk_i. \tag{2.28}$$

and by substituting k_i=$2\pi/\lambda$ into Equation 2.28

$$k_b' = \frac{4n\pi}{\lambda}. \tag{2.29}$$

For long wavelength acoustic phonons [9],

$$\omega' = v_b k_b' \tag{2.30}$$

where v_b is the bulk phonon velocity (either quasi-transverse or quasi-longitudinal). Substituting Equation 2.29 into Equation 2.30 givies

$$\omega' = \frac{4n\pi v_b}{\lambda} \tag{2.31}$$

where n is the refractive index of the probed material. Thus, the Brillouin frequency shift for bulk modes using backscattering geometry is given by.

$$f_b = \frac{2nv_b}{\lambda}, \tag{2.32}$$

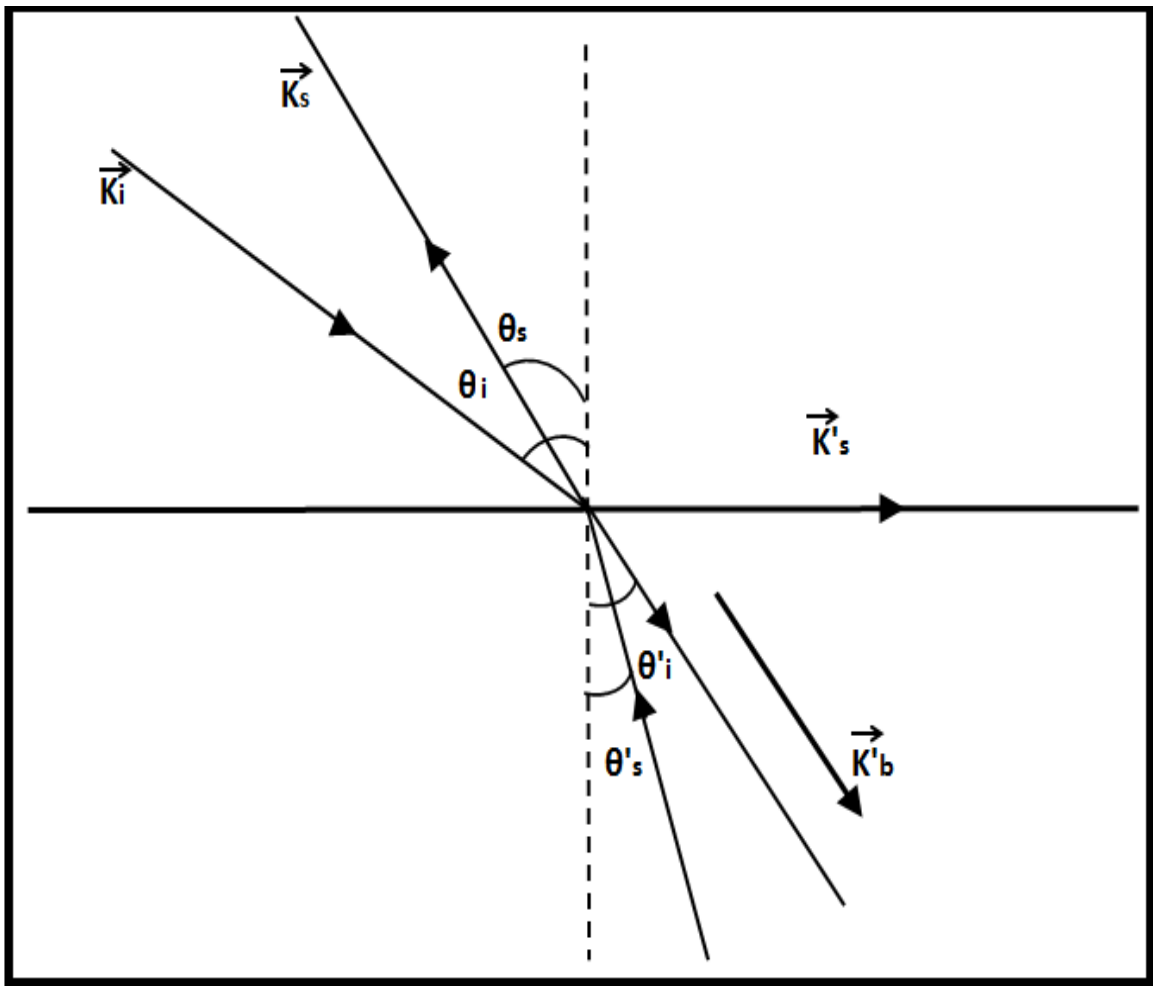

Figure 2.5: Brillouin light scattering from a medium, where k_i is the wavevector of the incident photon, k_s is the wave vector of the scattered photon, k_b' is the wavevector of the bulk phonon, k_s' is the wavevector of the surface phonon, θ_i is the angle between the surface normal and the incident photon, θ_s is the angle between the surface normal and the scattered photon, θ_s' is the angle between the surface normal and the refracted scattered photon, θ_i' is the angle between the surface normal and the refracted incident photon.

Chapter 3

Experimental Details

3.1 Introduction

In this chapter, the process used to synthesize the single crystals of Bi_2Se_3, Bi_2Te_3 and Sb_2Te_3 will be presented. This will be followed by a description of the the optical system used for the Brillouin light scattering experiments, including a detailed discussion of the tandem Fabry-Perot Interferometer used to analyze the scattered light.

3.2 Sample Fabrication

The samples of Bi_2Se_3, Bi_2Te_3 and Sb_2Te_3 used in this work were prepared by T. Sasagawa research group at Tokyo Institute of Technology using a process detailed in reference [42]. In summary, a modified Bridgman technique was used to grow a single crystals of Bi_2Se_3, Bi_2Te_3, and Sb_2Te_3. High purity and stoichiometric amounts of the constituent elements were sealed in evacuated quartz ampoules. This mixture was completely melted at T > 950 ^oC. To assure a homogeneneous mixture, the ampoules

were mechanically shaken and then cooled slowly in order to grow a single crystal. The resulting crystals were cleaved perpendicular to the c-axis, exposing a flat and shiny surface with a size of approximately 5 x 30 mm^2.

As can be seen in Equation (2.32), in order to determine the bulk phonon velocities and elastic constants of Bi_2Se_3, Bi_2Te_3 and Sb_2Te_3, the mass densities and refractive indices are required. The mass densities of Bi_2Se_3, Bi_2Te_3 and Sb_2Te_3 at room temperature were obtained from references [43, 44, 45], respectively. Refractive indices at 532 nm were estimated from plots of photon energy vs refractive index as in reference [46, 47, 48], and wavelength vs refractive index as in reference [49]. It should be noted that there are two values of refractive index in Table 3.1 for Sb_2Te_3. The implications of this will be discussed later in page 53. Table 3.1 summarizes these values.

Table 3.1: Densities and refractive indices (at 532 nm) of Bi_2Se_3, Bi_2Te_3, and Sb_2Te_3.

Material	Density (g/cm^3)	Refractive index
Bi_2Se_3	6.82 [43]	1.8 [46]
Bi_2Te_3	7.70 [45]	2.3 [47]
Sb_2Te_3	6.50 [44]	3.6 [49]
Sb_2Te_3	-	1.6 [48]

3.3 Optical System

Figure 3.1 shows a schematic diagram of the optical system used in this work. A photograph of this system is shown in Figure 3.2. The source of light used was a Coherent Verdi-V2 diode pumped Nd:YVO4 laser. The beam that is generated by the laser has a wavelength of 532 nm, bandwidth of ~10 MHz and is vertically polarized.

The output laser power is set to 2 W but had to be reduced substantially using absorbing (F1, F2) and variable neutral density (VNDF) filters to prevent damage to the sample. A half wave plate (HWP) was used to rotate the vertically polarized beam from the laser to a horizontally polarized beam. This horizontally polarized beam goes through a beam splitter (BS) which splits it into two beams. The reflected beam serves as a reference beam and enters the Fabry-Perot interferometer after reflection from mirror (M2). This beam is used to maintain Fabry-Perot mirror alignment, and helps to prevent the saturation of the photomultiplier tube by providing a beam while scanning over the region of the spectrum in which elastic scattering from a sample occurs near 0 GHz (scattered light from sample blocked by a shutter on the FPI entrance pinhole). The portion of the beam that is transmitted through the beam splitter strikes mirror (M1) and is subsequently directed toward prism (P). The light then undergoes total internal reflection in the prism to change its direction by 90^o, after which it is focused on the sample (S) using lens (L1) with focal length of 5 cm. Besides focusing light on the sample, this lens also collects the scattered light from the sample along a direction 180^o from the incident light direction. Another lens (L2) is also used to focus the scattered light onto the 450 nm entrance pinhole of the Fabry-Perot interferometer.

The Fabry-Perot interferometer is used extensively in Brillouin Spectroscopy experiments due to the high resolution it provides [50]. Basically, a FPI consists of two highly-reflecting mirrors aligned so that their surfaces are parallel to one another, one of the mirrors is fixed and the other is movable and they are separated by a distance d [51]. These two mirrors can be plane, as in the present experiments, or curved depending on the application.

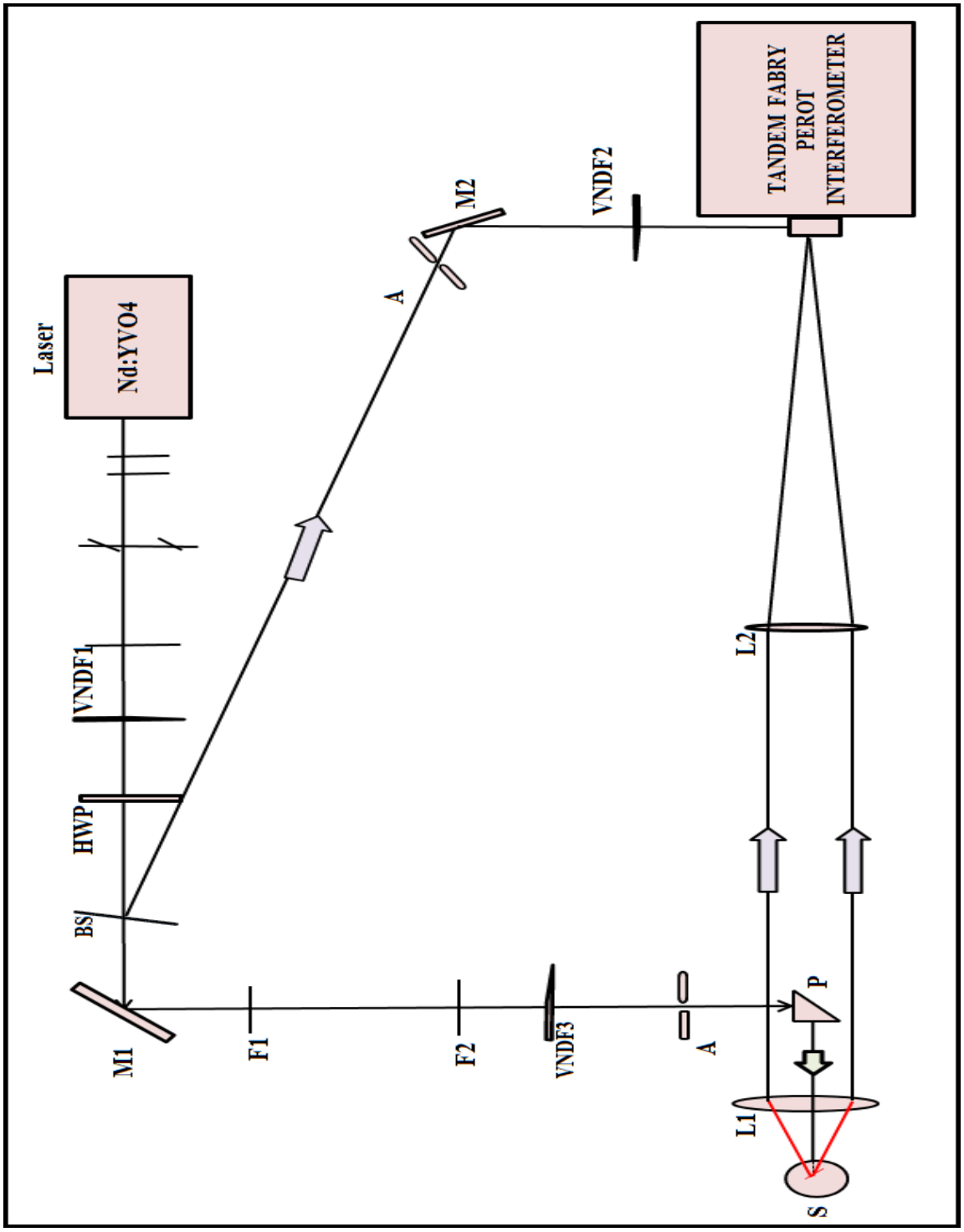

Figure 3.1: Schematic diagram of experimental set up. VNDF - Variable Neutral Density Filter, F - Filter, A - Aperture, HWP - Half Wave plate, P - Prism, L - Lens, BS - Beam Splitter, M - Mirror, S - Sample.

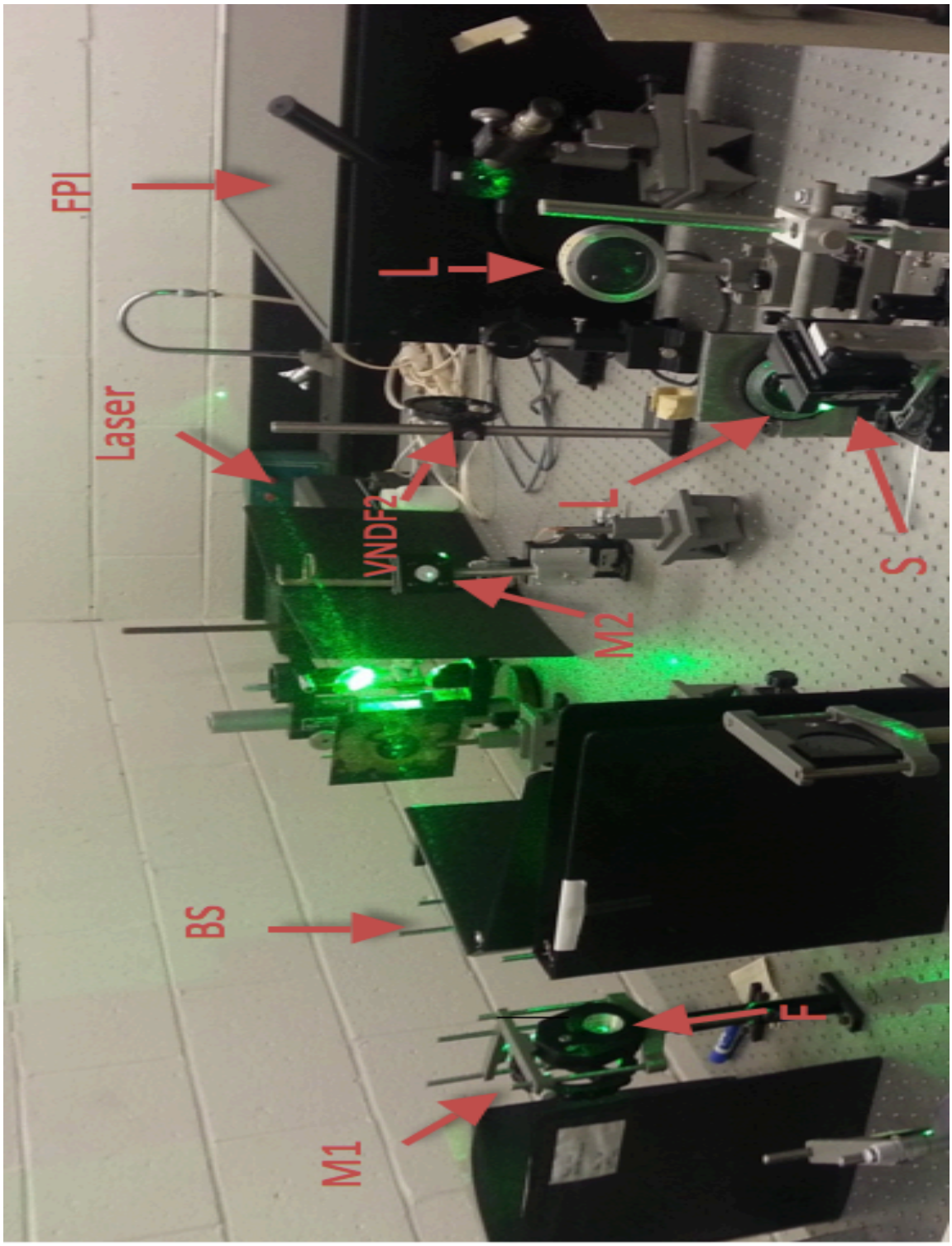

Figure 3.2: Photograph of Brillouin Scattering apparatus. VNDF - Variable Neutral Density Filter, F - Filter, L - Lens, BS - Beam Splitter, M - Mirror, S - Sample.

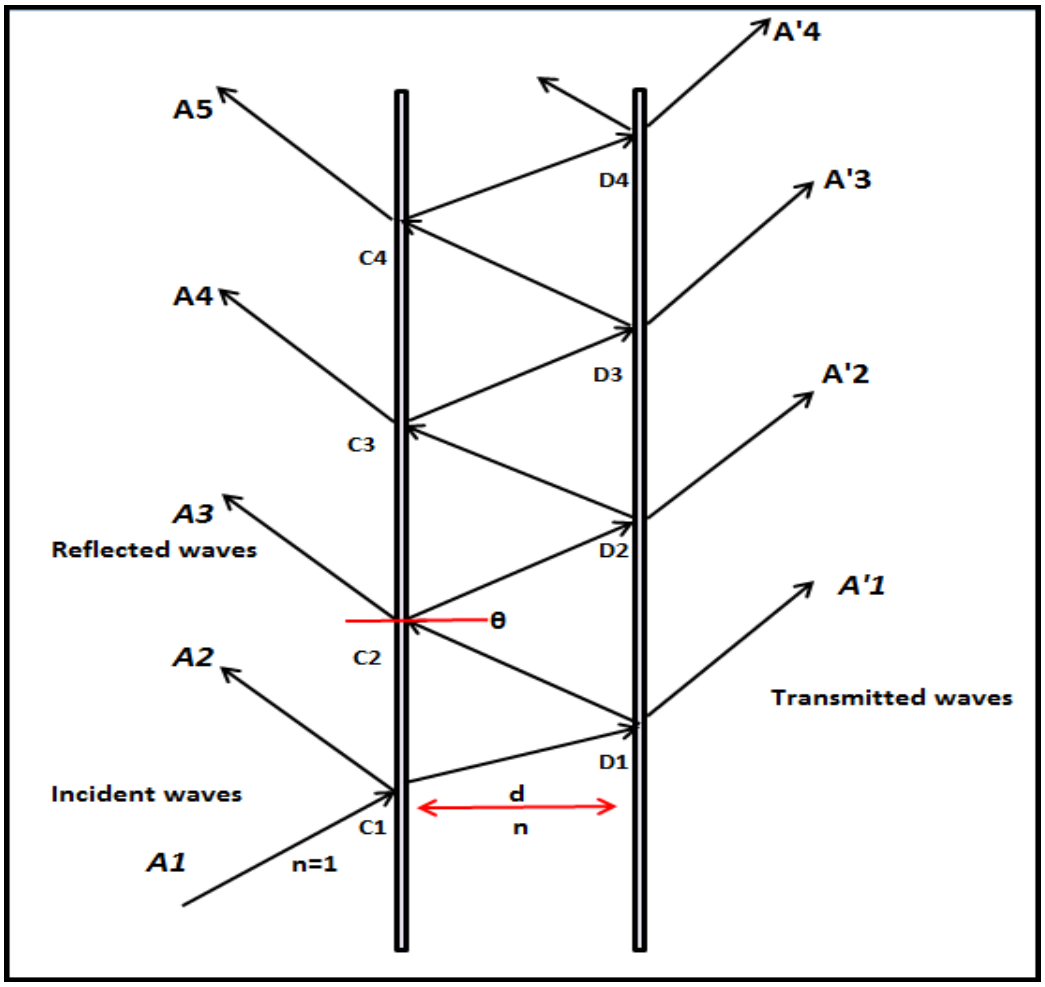

Figure 3.3: Internal reflections between mirrors separated by a distance d in the FP. d is the distance between mirrors, n is the refractive index, and θ is the angle between the surface normal to the plate and the reflected wave.

As shown in Figure 3.3, a beam incident on a FPI at angle of incidence θ undergoes multiple internal reflections between the two mirrors [52]. At the first mirror, the wave is divided into two waves, one is reflected in the direction C_1A_2 and the second wave is transmitted to the mirror in the direction C_1D_1. This second wave is incident on the second surface at angle θ and is then divided into two waves, one is transmitted in the direction D_1A_1', and the other wave is reflected back in the direction D_1C_2. This process of division of the wave continues as shown in Figure 3.3 [53]. A peak in transmission occurs only when the interference between waves is constructive. Constructive interference for normal incidence occurs when the following condition is satisfied:

$$m\lambda = 2nd \tag{3.1}$$

where d is the distance between the mirrors, λ the wavelength, m is an integer, and n is the refractive index of the medium between the mirrors.

Two important quantities pertaining to FPIs are the free spectral range (FSR) and the finesse F. The FSR is the spacing in optical frequency range between two adjacent transmission maxima as shown in Figure 3.4. and it is given by [54]

$$FSR = \frac{c}{2d} \tag{3.2}$$

where c is the speed of light in vacuum. In the present work, the FSR was in the range of 10-150 GHz.

The finesse (F) is defined as the ratio between the free spectral range and the instru-

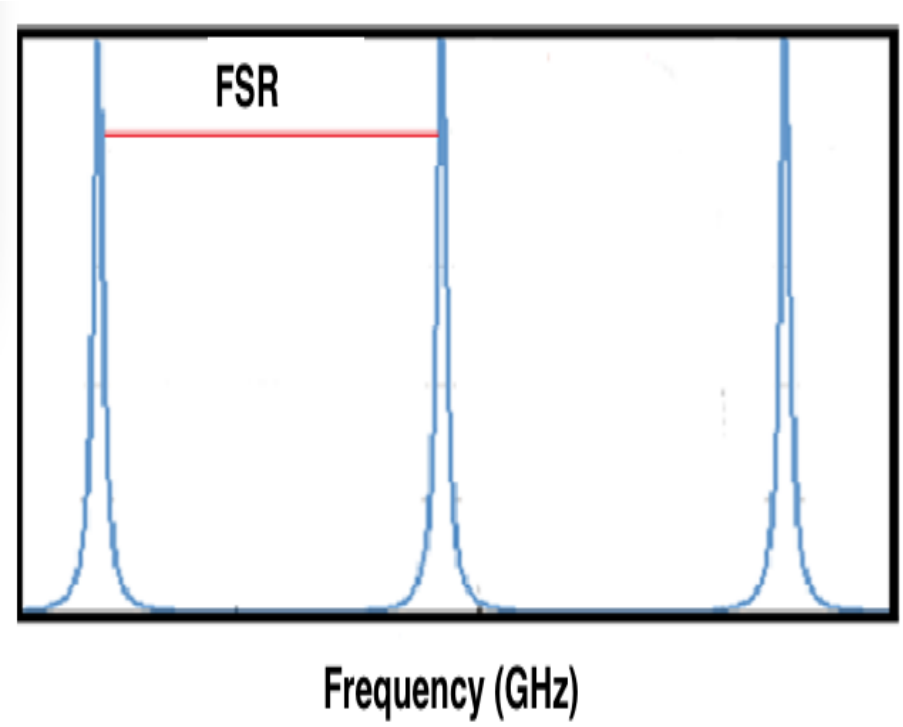

Figure 3.4: Free Spectral Range (FSR) of a Fabry-Perot Interferometer.

mental peak linewidth (δF) as expressed below [55].

$$F = \frac{FSR}{\delta F} \tag{3.3}$$

It was approximately ≈ 100 for the present work.

The FPI used in these studies is a Sandercock type, 6-pass tandem FPI (see Figure 3.5). The beam passes through each interferometer three times. The reason for utilizing two Fabry-Perot interferometers in one system is to increase the contrast which allows weak signals to be observed. Furthermore, another advantage of coupling two interferometers is that they provide a useful means for increasing the FSR while a fixed resolution is achieved [56].

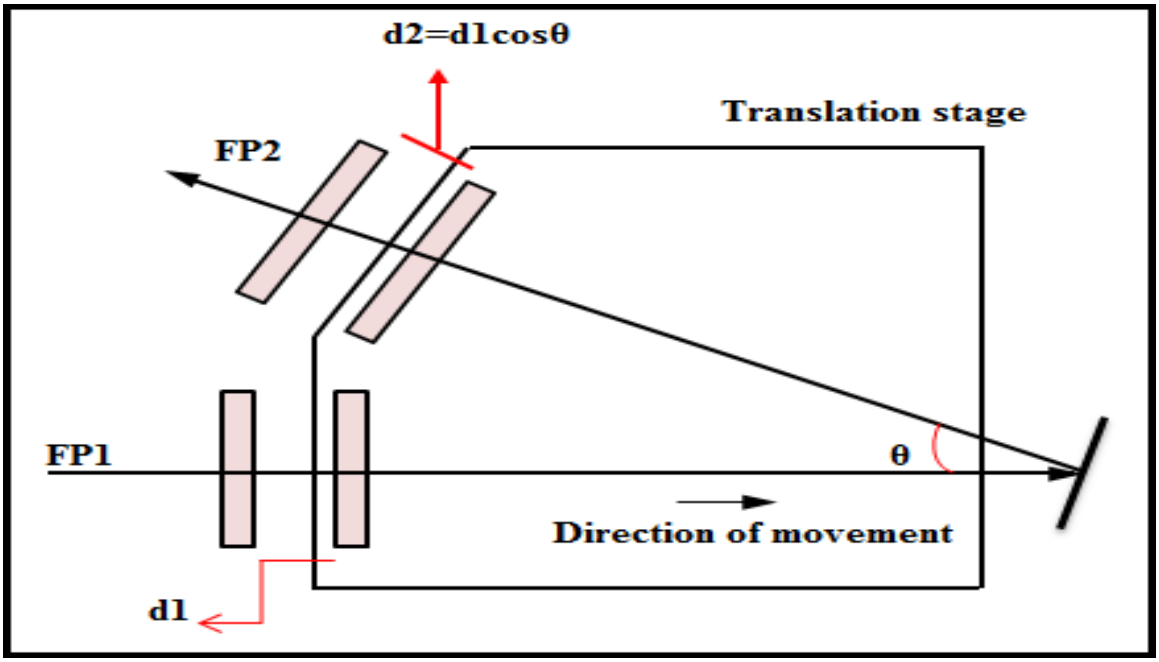

Figure 3.5: Two Fabry-Perot interferometers (Tandem) as used in the present experiments.

The two Fabry-Perot interferometers used in the tandem FPI are identical, with the exception that the distance between the two mirrors in the first cavity is slightly different from the second cavity. The mathematical relationship linking the distances between mirrors in each cavity is d_2=d_1 cos θ. One mirror in each cavity is fixed and the other mirrors are movable. The movable mirrors are placed and positioned on a common platform. Therefore, moving this platform causes the two mirrors to move simultaneously allowing frequency analysis of light incident on it. Although the spacing between the two mirrors is slightly different, both interferometers must satisfy Equation (3.1), then it can be seen that

$$2d_1 = p\lambda \tag{3.4}$$

and

$$2d_2 = q\lambda \tag{3.5}$$

where p and q are integers, and d_1, d_2 are the spacings between the mirrors of the two interferometers [57]. By applying these equations, one can eliminate the repetition of transmission maxima, (unlike as found for a single interferometer) as seen in Figure 3.6. From equations (3.4) and (3.5), it can be shown that the change in spacing for both interferometers must also satisfy the following equation:

$$\frac{\delta d_1}{\delta d_2} = \frac{d_1}{d_2}. \tag{3.6}$$

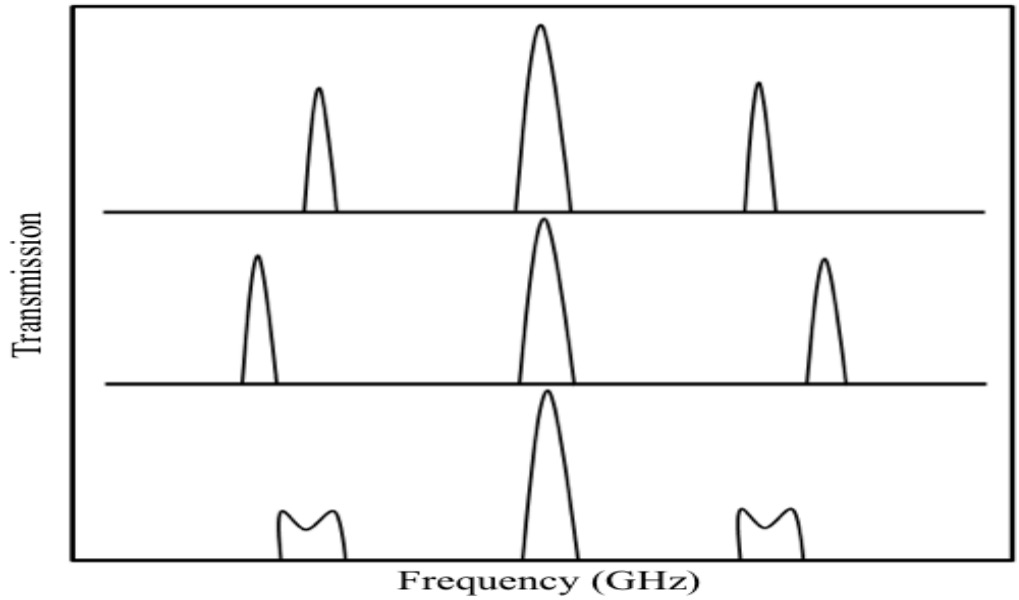

Figure 3.6: Two Fabry-Perot interferometers (Tandem) as used in the present experiments to avoid a repetition of maxima.

Figure 3.7 shows the path of the beam that is incident on the entrance pinhole of the FPI. This beam is then incident on a mirror (M1). Light reflecting from M1 is collected by a lens (L1) and is incident on another mirror (M2). This mirror ensures that beam is normally incident on the first Fabry-Perot mirrors and at the proper position. Subsequently, the light passes through an aperture (A2) and is then incident on another mirror (M3), which directs the beam to the second Fabry-Perot interferometer. Once the beam leaves the second Fabry-Perot interferometer, it hits a prism (P1) and returns parallel to its direction. This means that the beam will enter the second Fabry-Perot interferometer again, hitting (M3), going through an aperture (A2) and entering the first Fabry-Perot again. The beam that exits the first Fabry-Perot is incident on M2. Then, a focusing lens (L1) focuses the beam on (M4). Due to the vertical displacement as a result of the 90^o prism, the beam will not be incident on M1. The beam then strikes both Fabry-Perot interferometer once more

before hitting mirror (M5). This mirror reflects the beam towards a prism (P2). Then the beam is incident on (M6) whose role is to reflect the beam into an aperture (A3), lens (L2), the pinhole and then to photomultiplier. The information obtained is then displayed by the computer [57].

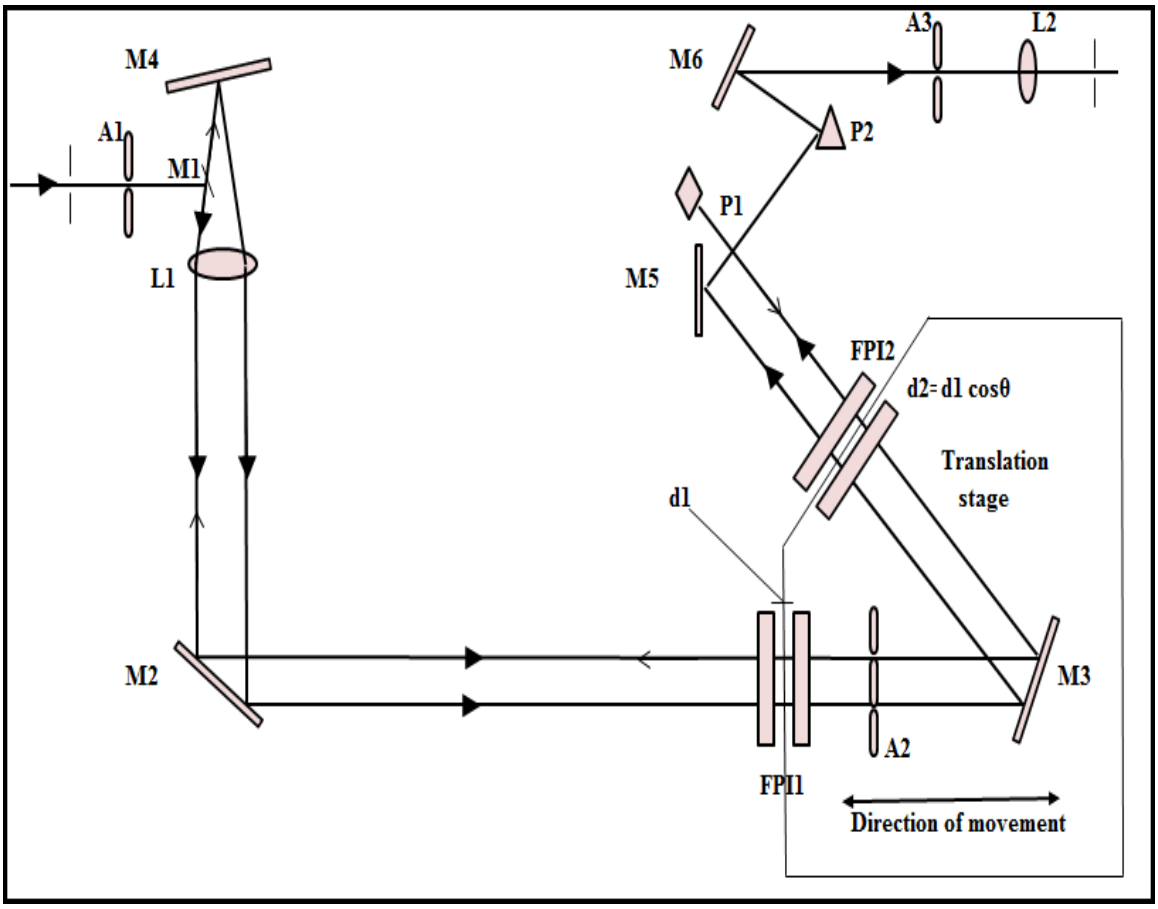

Figure 3.7: The process inside the Fabry-Perot interferometer in which the light passes each FPI three times. FPI - Fabry Perot Interferometer, d - distance between mirrors, A - Aperture, P - Prism, L - Lens, M - Mirror.

As the alignment of the Fabry-Perot can be affected by temperature and humidity, the system must be actively stabilized. The stabilizing control helps maintain both the parallel alignment of the mirrors used in the interferometer as well as the spacing between mirrors. This is accomplished by control electronics which apply voltage to piezoelectric crystals to tilt the mirrors so that they remain parallel to one another, and also to scan the mirror spacing.

3.4 Laser Beam-Induced Sample Damage

Preliminary Brillouin scattering experiments on Bi_2Se_3 yielded unusual spectra. Polarization studies were done to see if the presence of Brillouin peaks in spectra depended on polarization state, as is normally the case. Unfortunately, no changes were observed in the spectrum at all when the scattered light from the sample was vertically and horizontally polarized. This led us to examine the sample by the microscope, and it was found that the sample was damaged due to the high intensity of the incident beam ($\approx$ 40 mW) (see Figures 3.8 and 3.9). After that, each result was verified by conducting vertical and horizontal polarization studies on the scattered light, as well as checking the sample with the microscope to be confident about all results obtained. The beam power was therefore set to 10 mW for all experiments. This power level still allowed spectra of reasonable quality to be obtained.

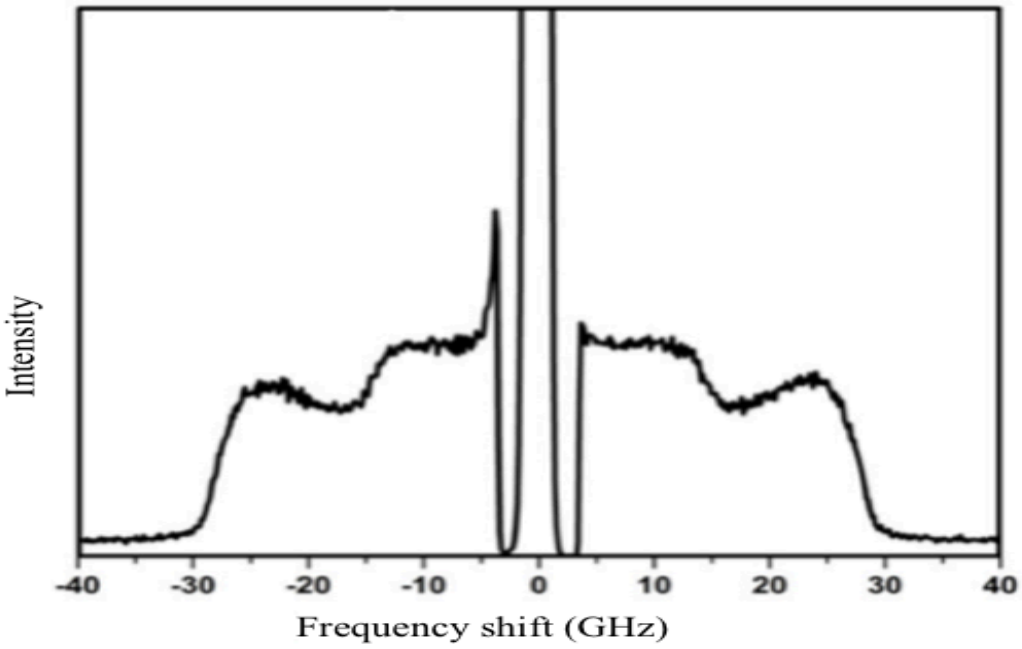

Figure 3.8: Brillouin spectrum of sample of Bi_2Se_3 damaged by incident laser beam.

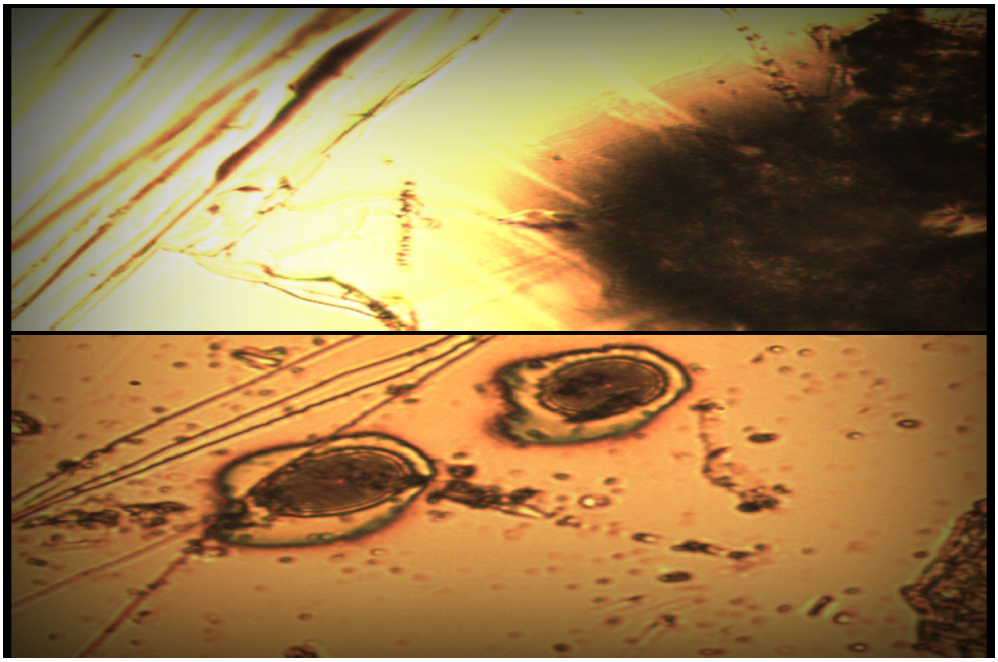

Figure 3.9: A photo of a damaged sample by 40 mW incident beam intensity.

Chapter 4

Results and Discussion

4.1 Introduction

Brillouin spectra were obtained from two samples each of Bi_2Se_3, Sb_2Te_3, and Bi_2Te_3. Surface and bulk acoustic phonon velocities were obtained from the Brillouin peak frequency shifts. Corresponding elastic constants were also estimated from the acoustic phonon velocities and by knowing the material densities.

4.2 Bismuth Selenide (Bi_2Se_3)

Figures 4.1 and 4.2 show spectra collected from sample Bi_2Se_3-1 and Bi_2Se_3-2, respectively, for various angles of incidence and an FSR of 15 GHz. One set of Brillouin peaks is observed which is labelled R. It can be seen that the frequency shift of this peak increases with increasing angle of incidence. Since it was expected that Brillouin peaks due to bulk modes might appear at higher frequency shifts, the FSR was increased to 30 and also 50 GHz so that peaks at high frequency can be observed. Figure 4.3 shows Brillouin spectra of Bi_2Se_3-1 collected at an FSR of 30 GHz. Three

sets of Brillouin peaks are observed: they are labelled T_1, T_2, and L. It can be seen that changing the angle of incidence does not change the frequency shift of these peaks except for L peak at 70^o which shows some variation in shift with angle. The magnitude of this variation is unexpected because the range of external incident angles used is 35^o which corresponds to a small range of directions (10^o) probed inside the material. That is, the bulk phonons that were probed travelled in directions from 21^o to 31^o from the z-axis. It should be noted that no peaks analogous to the T_1, T_2, and L were observed in spectra of sample Bi_2Se_3-2. The reason for this is unclear, but it could be related to sample opacity. Bi_2Se_3-2 was also examined at higher frequency shifts from (30 - 150 GHz) and no additional Brillouin peaks were observed.

Even though many of the experiments were done several times, the same poor quality of peaks were observed. It might be due to the low intensity of incident light used. Accordingly, the uncertainty in the frequency shift has been estimated to be ± 0.3 GHz. The frequency shifts of all peaks are presented in Table 4.1.

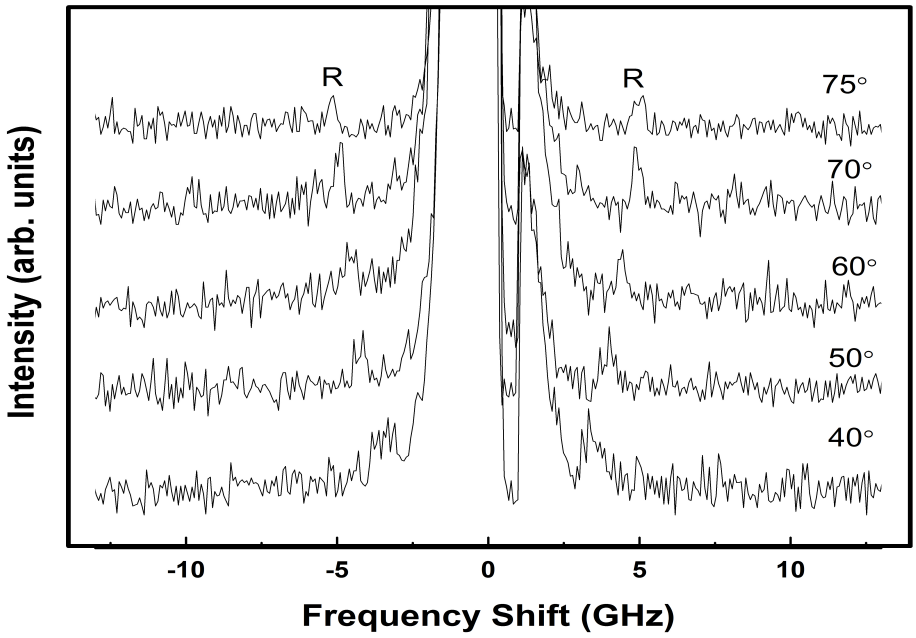

Figure 4.1: Brillouin spectra of Bi_2Se_3-1 collected at various angles of incidence. The free spectral range was set to 15 GHz.

.

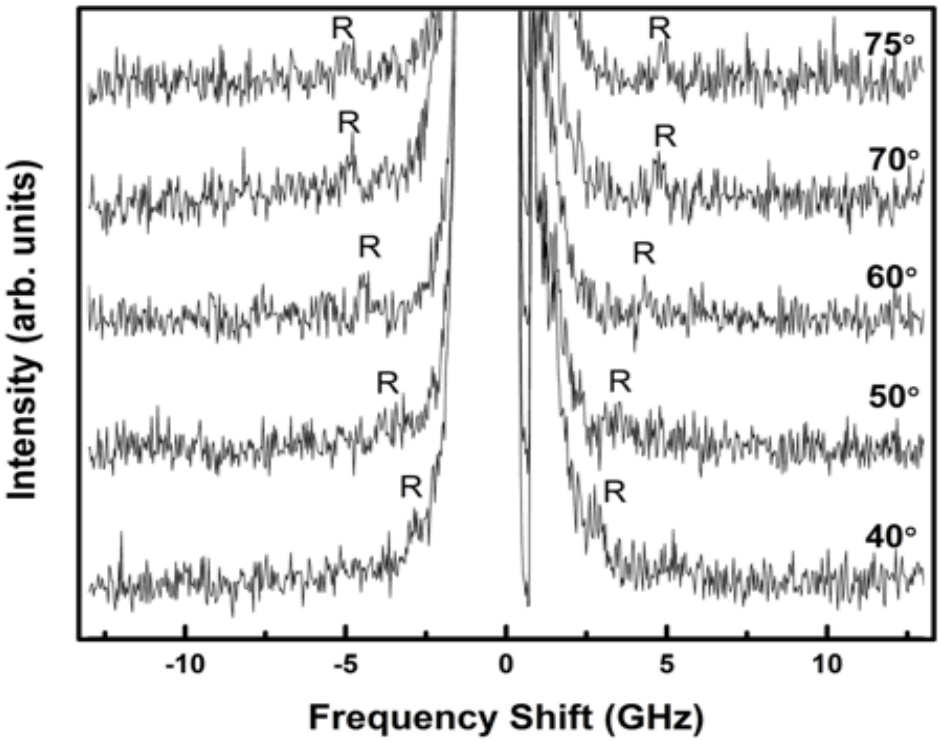

Figure 4.2: Brillouin spectra of Bi_2Se_3-2 collected at various angles of incidence. The free spectral range was set to 15 GHz.

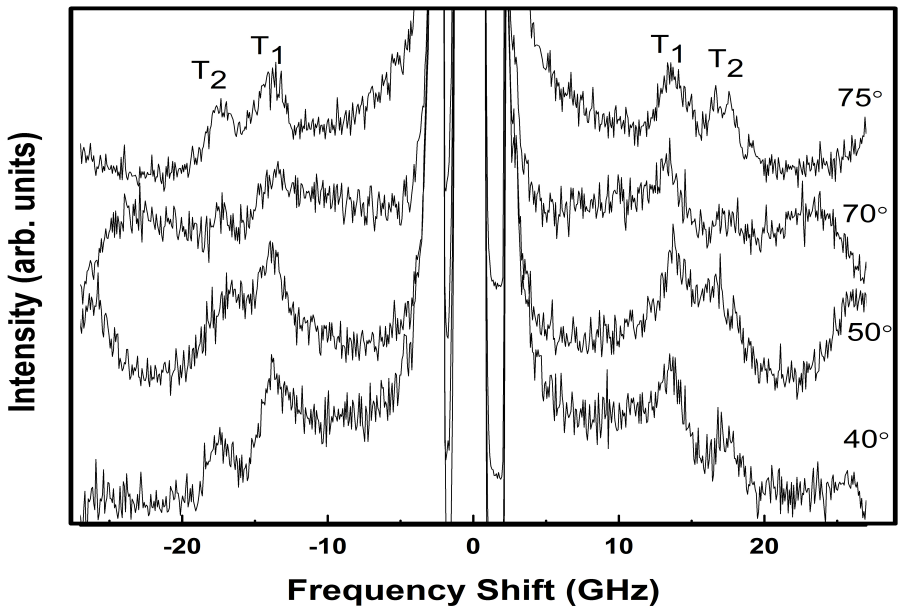

Figure 4.3: Billouin spectra of Bi_2Se_3-1 collected at various angles of incidence. The free spectral range was set to 30 GHz.

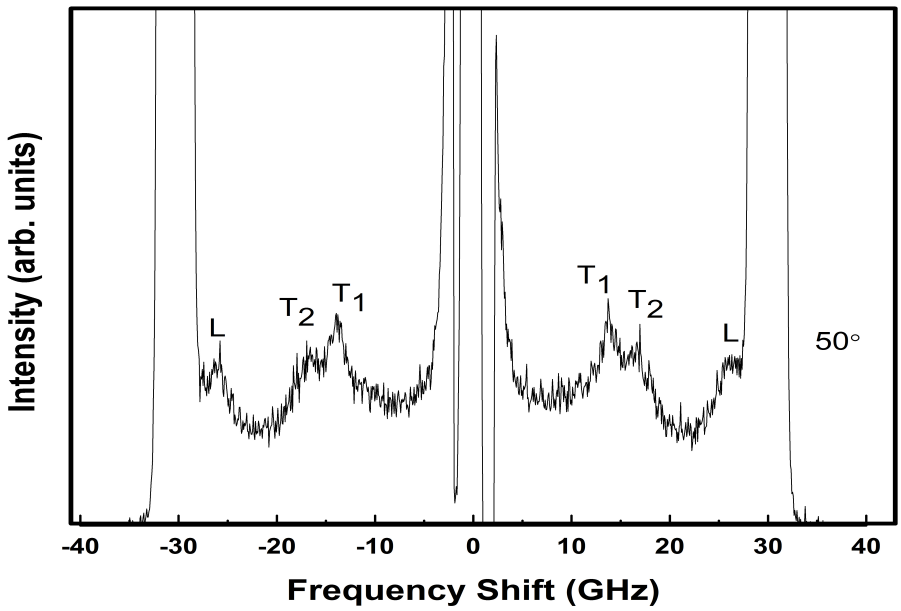

Figure 4.4: Billouin spectra of Bi_2Se_3-1 collected at 50^o of incidence. The free spectral range was set to 30 GHz.

Table 4.1: Average Brillouin frequency shifts for Rayleigh (R), quasi-transverse bulk (T_1, T_2), and quasi-longitudinal bulk (L) peaks of Bi_2Se_3-1 and Bi_2Se_3-2.

Sample	Angle of incidence ($\pm 1^o$)	f_R ($\pm$0.3 GHz)	f_{T_1} ($\pm$0.3 GHz)	f_{T_2} ($\pm$0.3 GHz)	f_L ($\pm$0.3 GHz)
1	40	3.3	13.6	17.3	25.8
	50	3.9	13.6	17.0	25.7
	60	4.4	-	-	-
	70	4.9	13.5	17.2	25.0
	75	5.1	13.5	17.3	25.8
2	40	3.0	-	-	-
	50	3.7	-	-	-
	60	4.5	-	-	-
	70	4.8	-	-	-
	75	5.1	-	-	-

Using the data in Table 4.1, the frequency shifts of R peak for Bi_2Se_3-1 and Bi_2Se_3-2 are plotted against sin θ as seen in Figures 4.5 and 4.6, respectively. It can be seen that the shift depends linearly on sine of the angle of incidence. Equation (2.21) fitted well to this data and confirmed that the R peak is due the Rayleigh surface mode. Polarization studies were also conducted on Bi_2Se_3-1, and Bi_2Se_3-2 as shown in Figures 4.7, and 4.8. With the incident light on the sample horizontally polarized, R peak disappeared with a vertical polarization (HV), and remained with a horizontal polarization (HH). The velocity of this mode, v_R, was extracted from the slope of the line of best fit and is given in Table 4.2.

The frequency shifts of the T_1, T_2 and L peaks were found to be relatively independent of sine of the angle of incidence as shown in Figure 4.5. This confirms that these peaks are due to bulk quasi-transverse and quasi-longitudinal acoustic modes. Using Equation (2.32) along with the average frequency shift data in Table 4.1 and the refractive index values presented in Table 3.1, the velocities of these modes, v_{T1}, v_{T2}, and v_L, were determined and are given in Table 4.2.

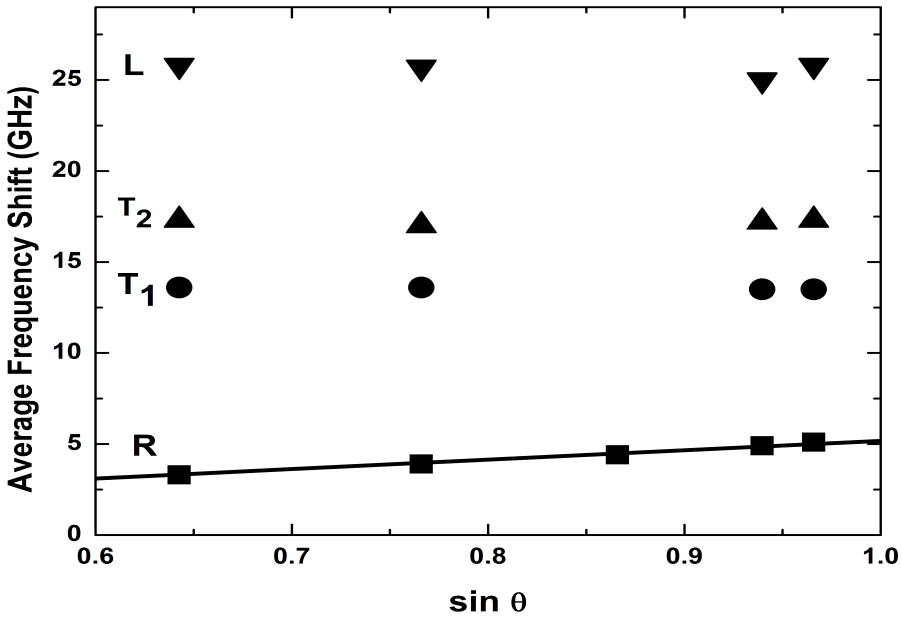

Figure 4.5: Average frequency shifts versus sine of incident angle for R, T_1, T_2, and L peaks in Brillouin spectra of Bi_2Se_3-1. δ^o=±1^o, δR= ±0.3 GHz, δT_1= ±0.3 GHz, δT_2= ±0.3 GHz, and δL= ±0.3 GHz, R^2= 0.992.

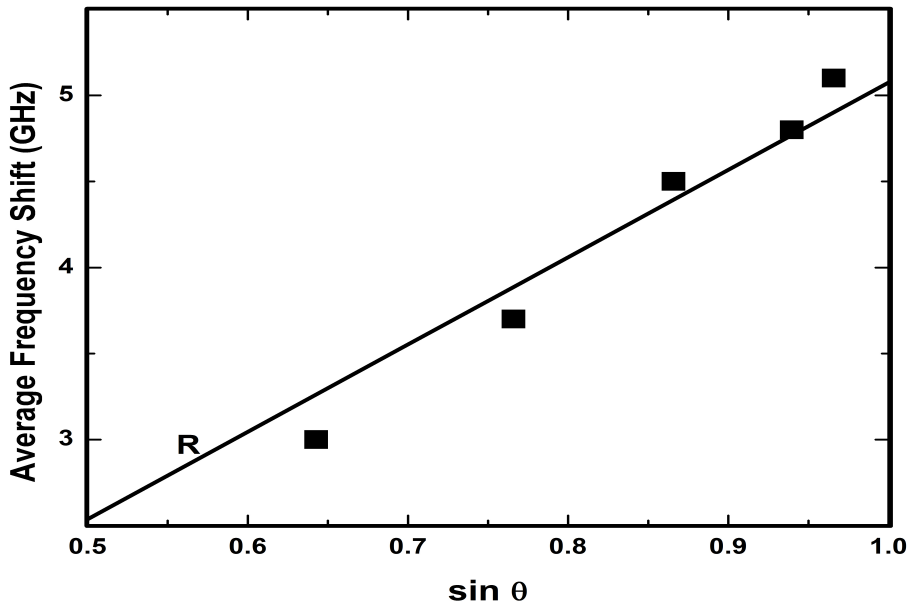

Figure 4.6: Frequency shift of R peak of Bi_2Se_3-2 versus sine of the angle of incidence. δ^o=±1^o, δR= ±0.3 GHz, R^2= 0.987.

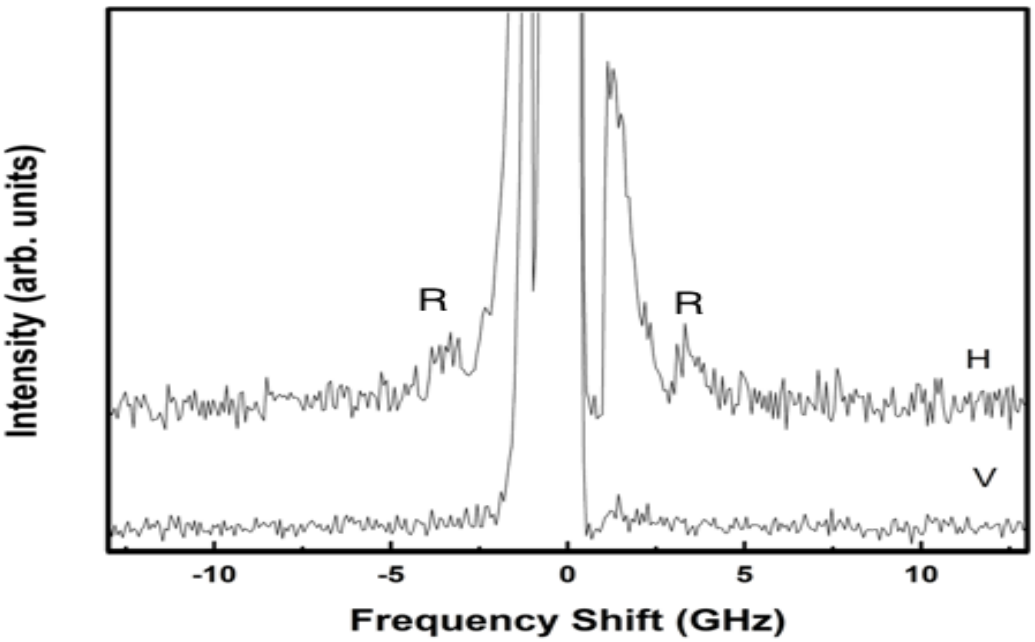

Figure 4.7: Brillouin spectra of Bi_2Se_3-1. V: vertically-polarized scattered light, H: horizontally-polarized scattered light. The incident light was horizontally polarized in both cases.

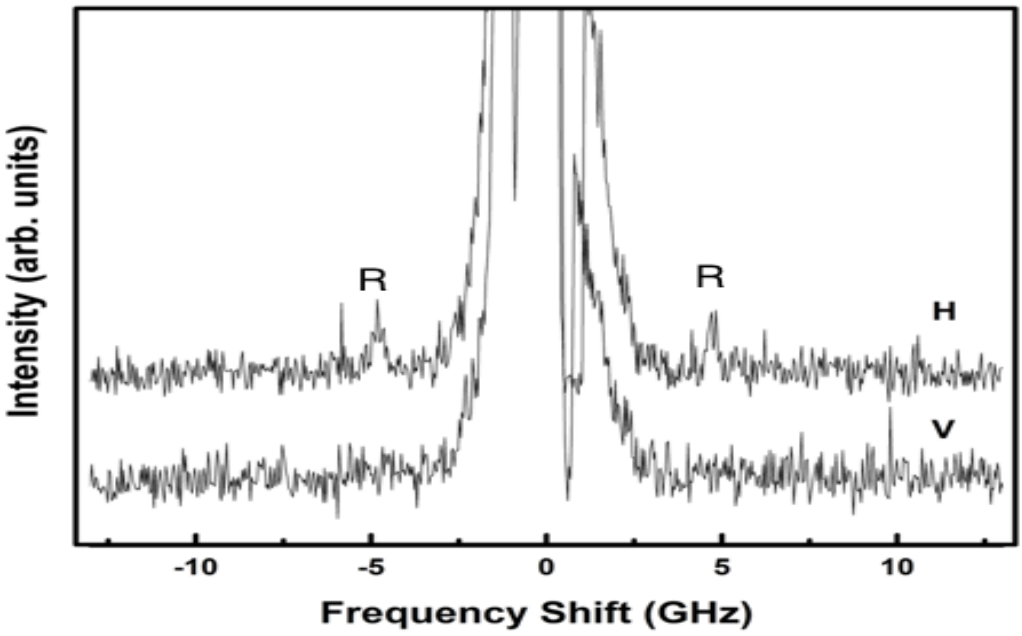

Figure 4.8: Brillouin spectra of Bi_2Se_3-2. V: vertically-polarized scattered light, H: horizontally-polarized scattered light. The incident light was horizontally polarized in both cases.

Table 4.2: Rayleigh surface, slow and fast quasi-transverse, quasi-longitudinal acoustic phonon velocities of Bi_2Se_3-1 and Bi_2Se_3-2.

Sample	v_R ($\pm 120\ m/s$)	v_{T1} ($\pm 100\ m/s$)	v_{T2} ($\pm 140\ m/s$)	v_L ($\pm 210\ m/s$)
1	1400	2000	2500	3800
2	1400	-	-	-

The Rayleigh surface phonon velocities (shown in Table 4.2) of the two samples of Bi_2Se_3 are in excellent agreement. Now, it is possible to estimate the elastic constants of Bi_2Se_3. Even though such materials have six independent elastic constants, it was possible to find two of them. This is because the phonons probed in the present experiments travel in directions close to the z-axis. The range of angle of incidence used results in a very small range of probed directions inside the material, and these directions are close to the z-axis direction. Knowledge of the T and L velocities along this direction allows only elastic constants C_{33} and C_{44} to be determined. Using Equation 2.10 and knowing the density, quasi-longitudinal velocity, C_{33} has been estimated to be 98 ±7 GPa. Since there are two values of the quasi-transverse velocity v_{T1} and v_{T2}, C_{44} has two values determined from those velocities. Using Equation 2.11 and knowing the density, C_{44} calculated from v_{T1} and v_{T2} has been estimated to be 29 ±2 GPa and 44 ±4 GPa, respectively. As a result, the average C_{44} was found to be 37 ±10 GPa.

4.2.1 Mechanical Exfoliation

Since it has been shown that changing the thickness of topological insulators Bi_2Se_3, Bi_2Te_3, and Sb_2Te_3 can result in changes in the intensity of Raman spectral peaks [58], it was thought that decreasing the thickness of the samples used in the present experiments might cause a change in the Brillouin spectra. For this reason, Bi_2Se_3 was exfoliated several times using normal tape resulting in samples of different thicknesses where each subsequent exfoliation resulted in a thinner sample. The sample was examined once after every exfoliation process, and after approximately three exfoliations the sample became too small to probe with laser beam.

Figure 4.9 shows Brillouin spectra collected from the thinnest mechanically exfoliated sample. It is evident, by comparison to Figure 4.1, that the spectra are qualitatively similar to those obtained from the non-exfoliated sample. Table 4.3 presents the average frequency shifts for various angles of incidence. The surface mode was seen with all thickness at similar frequency shifts as the original sample. This implies that the Brillouin frequency shifts are not affected by the material thicknesses at least down to the thicknesses studied here. Moreover, the quality of the spectra collected from the exfoliated material is very similar to those obtained from the sample in its original non-exfoliated state, even though one might expect spectra of higher quality due to the pristine nature of the exfoliated surface. Because no changes were observed in the spectra of the exfoliated samples of Bi_2Se_3-1, analogous experiments on Sb_2Te_3, and Bi_2Te_3 were not carried out. The exfoliated Bi_2Se_3-1 was examined at higher FSR (50-150 GHz), and no peaks were observed.

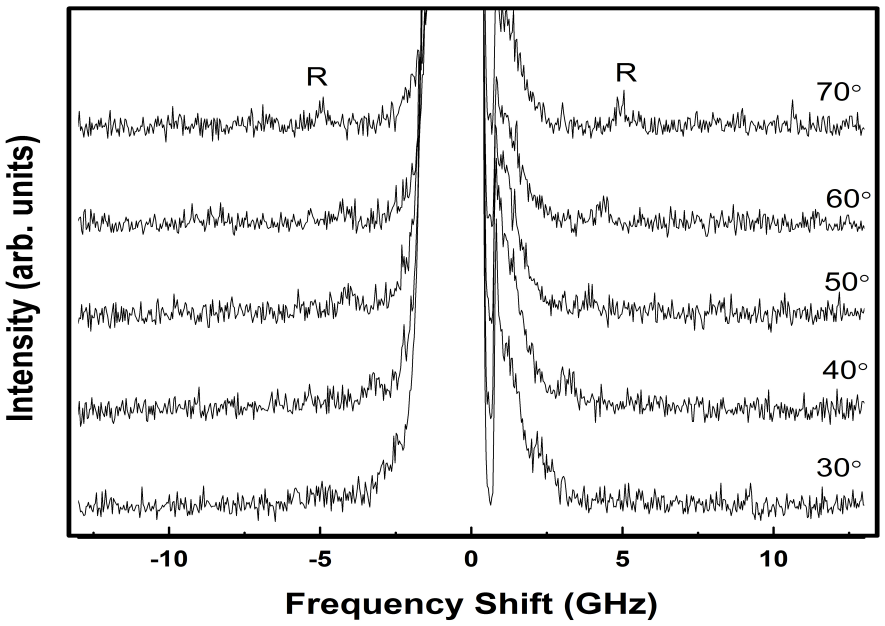

Figure 4.9: Billouin spectra of exfoliated Bi_2Se_3-1 collected at various angles of incidence. The free spectral range was set to 15 GHz.

Table 4.3: Average frequency shift of R peak along with corresponding angles of incidence for exfoliated Bi_2Se_3-1.

Angles of incidence ($\pm 1^o$)	Average Frequency Shifts ($\pm$ 0.3 GHz)
30	2.3
40	3.2
50	3.8
60	4.3
70	5.0

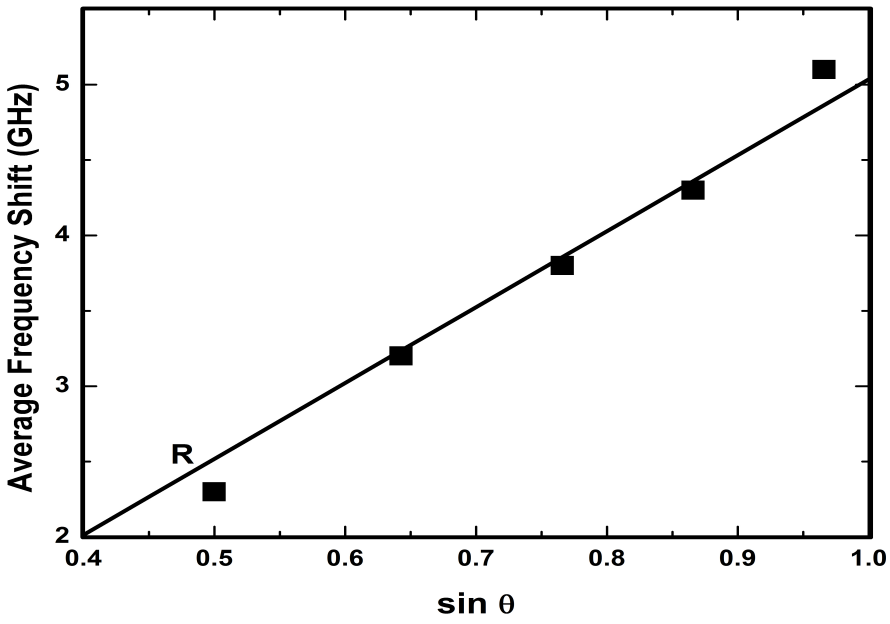

Figure 4.10: Average frequency shift of exfoliated Bi_2Se_3-1 versus sine of the angle of incidence. δ^o=±1^o, δR= ±0.3 GHz, R^2= 0.982.

Figure 4.10 shows the frequency shift of the R peak as a function of sin θ. It can be seen that the shift depends linearly on sin θ, fitting of Equation (2.21) yields a Rayleigh surface mode velocity v_R=1400 ± 100 m/s.

It can be seen from Table 4.4 that similar Rayleigh surface phonon velocities were obtained from exfoliated and non-exfoliated Bi_2Se_3. It is therefore concluded that, at least down to the values studied here, the sample thickness has a negligible effect on the Rayleigh surface mode velocity.

Table 4.4: Rayleigh surface phonon velocities of exfoliated Bi_2Se_3-1 and non exfoliated Bi_2Se_3-1.

Material	v_R ($\pm 120\ m/s$)
Non exfoliated	1400
Exfoliated	1400

4.3 Antimony Telluride (Sb_2Te_3)

Figures 4.11 and 4.12 show spectra collected from sample Sb_2Te_3-1 and Sb_2Te_3-2, respectively, for various angles of incidence from 40^o to 75^o with the FSR set to 15 GHz. In general, the spectra are of higher quality than those of Bi_2Se_3. One set of Brillouin peaks is seen which is labelled R. It can be seen that frequency shift of this peak increases when the angle of incidence is increased. After the data of R peaks were obtained at low free spectral range, it was expected that Brillouin peaks due to bulk modes might appear at higher frequency shifts. Accordingly, the spacing between mirrors in the Fabry-Perot interferometers was reduced to 3 mm which allows a higher frequency shift regime to be scanned. Figures 4.13 and 4.14 show spectra collected from sample Sb_2Te_3-1 and Sb_2Te_3-2, respectively, for various angles of incidence from 30^o to 60^o with an FSR of 50 GHz in order to see if there are peaks at higher frequency shifts. One set of Brillouin peak was observed which is labelled L. Since the range of angles used was small, the range of directions probed inside the material was found to be 11^o. That is, the bulk phonons that were probed travelled in directions from 23^o to 34^o from the z-axis. Accordingly, changing the angle of incidence caused a very slight difference in the frequency shifts of L peak.

Table 4.5 shows the average frequency shifts of both R and L peaks for different angles of incidence.

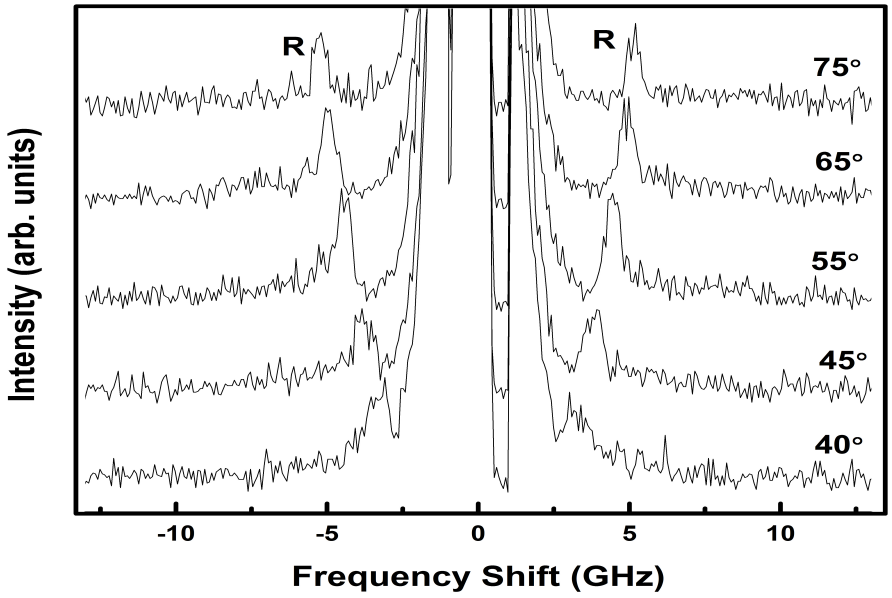

Figure 4.11: Billouin spectra of Sb_2Te_3-1 collected at various angles of incidence. The free spectral range was set to 15 GHz.

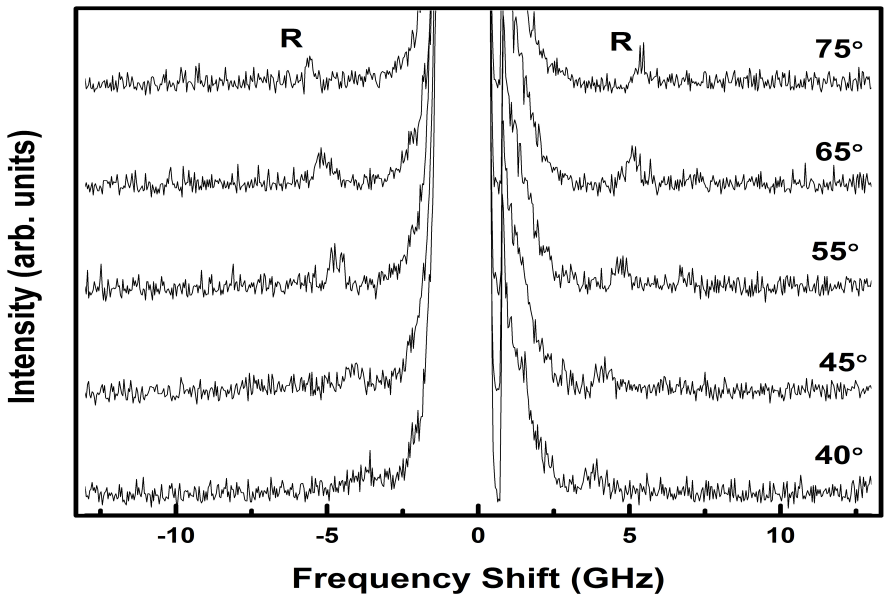

Figure 4.12: Billouin spectra of Sb_2Te_3-2 collected at various angles of incidence. The free spectral range was set to 15 GHz.

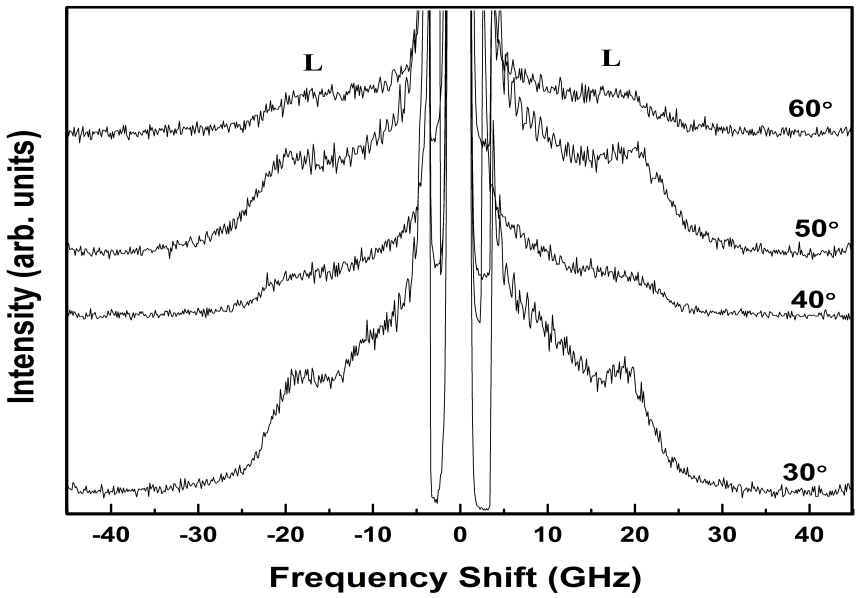

Figure 4.13: Billouin spectra of Sb_2Te_3-1 collected at various angles of incidence. The free spectral range was set to 50 GHz.

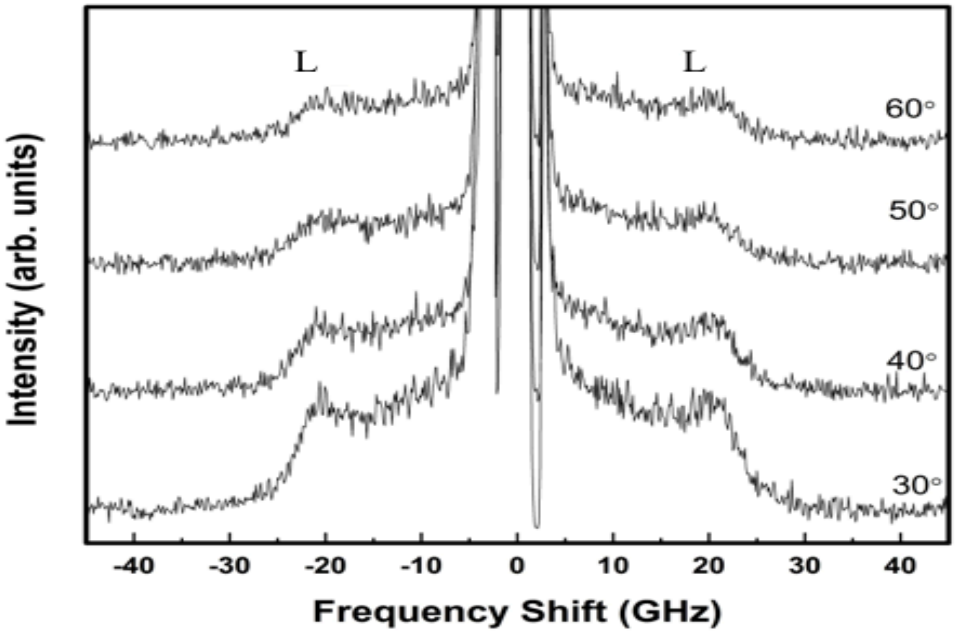

Figure 4.14: Billouin spectra of Sb_2Te_3-2 collected at various angles of incidence. The free spectral range was set to 50 GHz.

Table 4.5: Average frequency shifts of f_R and f_L of Sb_2Te_3-1 and Sb_2Te_3-2

Sample	Angle of incidence ($\pm 1^o$)	f_R (± 0.2 GHz)	f_L (± 0.2 GHz)
1	40	3.2	18.9
	50	3.8	18.7
	60	4.4	19.0
	70	4.9	18.9
	75	5.1	19.0
2	40	3.7	20.7
	50	4.1	20.6
	60	4.7	20.4
	70	5.1	20.5
	75	5.3	20.4

Using the data in Table 4.5, the frequency shift of the R peak for Sb_2Te_3-1 and Sb_2Te_3-2 are plotted against sine θ as shown in Figures 4.15 and 4.16, respectively. It can be seen that the shift depends linearly on sine of the angle of incidence. Equation (2.21) fitted well to this data and confirmed that R peak is due to the Rayleigh surface mode. Polarization studies were also conducted on Sb_2Te_3-1 and Sb_2Te_3-2 as shown in Figures 4.17 and 4.18, respectively. With the incident light on the sample horizontally polarized, R peak disappeared with a vertical polarization (HV), and remain with a horizontal polarization (HH). The velocities of this mode, v_R, was extracted from the slope of the line of best fit and is given in Table 4.6.

The frequency shift of the L peak was found to be relatively independent of sine of the angle of incidence as shown in Figures 4.15 and 4.16. This confirms that this peak is due to bulk quasi-transverse or quasi-longitudinal acoustic mode. Polarization studies were also conducted on Sb_2Te_3-1 and Sb_2Te_3-2 at a small angle ($< 20^o$) to assure the character of this peak as shown in Figures 4.19 and 4.20, respectively. With the incident light on the sample horizontally polarized, the L peak disappeared when a vertical polarization (HV) was applied on the scattered light from the sample,

and remain with a horizontal polarization (HH) confirming the character of L peak to be due to bulk quasi-longitudinal mode. Using Equation (2.32) along with the average frequency shift and the refractive index presented in Table 3.1, the velocity of this mode, v_L, was determined and is given in Table 4.6. It should be noted that the value of v_L presented in Table 4.6 was determined from Equation (2.32) using the refractive index in reference [48]. A second value of refractive index [49] yielded a quasi-longitudinal bulk phonon velocity that is much smaller than that presented in Table 4.6 and much smaller than the quasi-longitudinal velocities for Bi_2Te_3 and Bi_2Se_3. For this reason, it was not used in our velocity calculations.

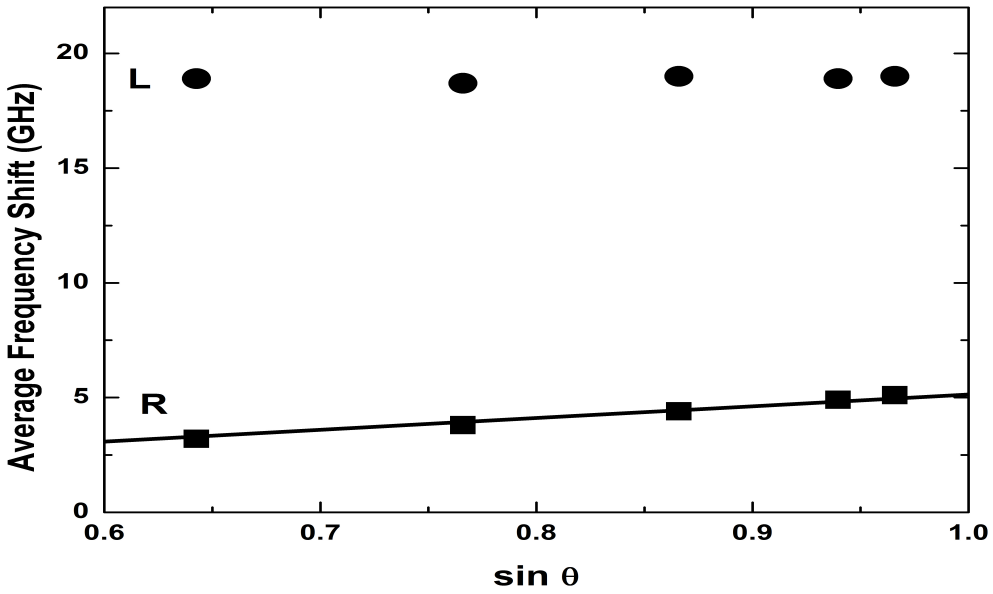

Figure 4.15: Frequency shifts of Brillouin peaks versus sine of the angle of incidence for sample Sb_2Te_3-1. δ^o=±1^o, δR= ±0.2 GHz, and δL= ±0.2 GHz, R^2= 0.994.

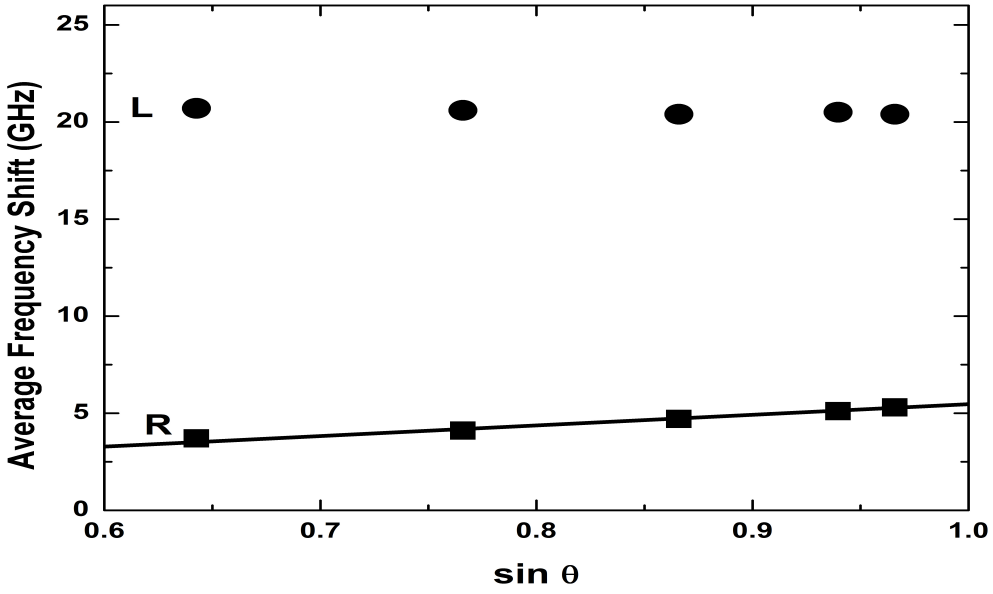

Figure 4.16: Frequency shifts of Brillouin peaks versus sine the angle of incidence for sample Sb_2Te_3-2. δ^o=±1^o, δR= ±0.2 GHz, and δL= ±0.2 GHz, R^2= 0.988.

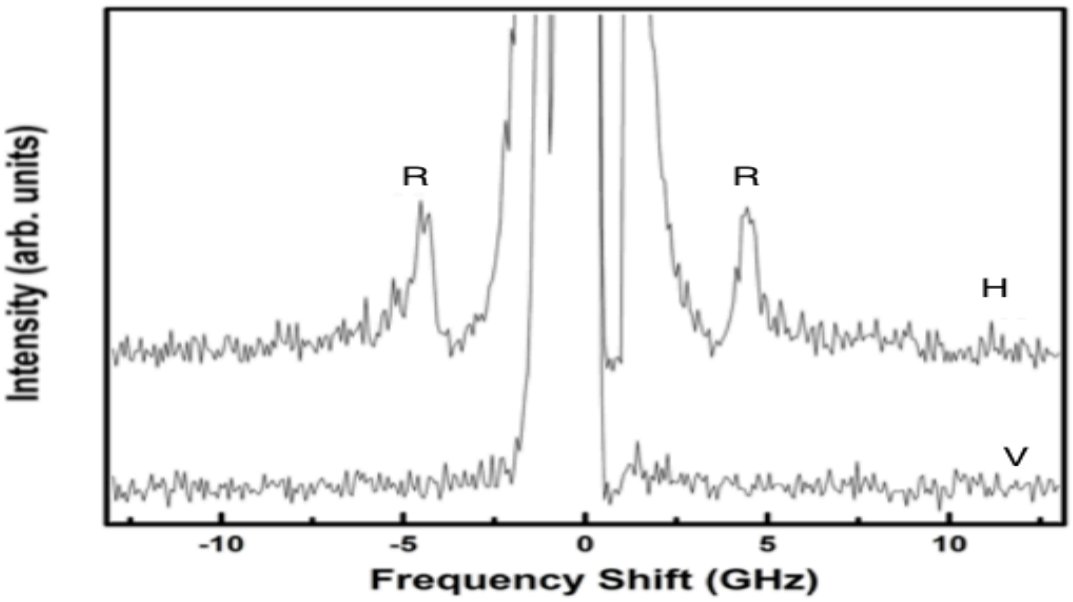

Figure 4.17: Brillouin spectra of Sb_2Te_3-1. V: vertically-polarized scattered light, H: horizontally-polarized scattered light (H). The incident light was horizontally polarized in both cases.

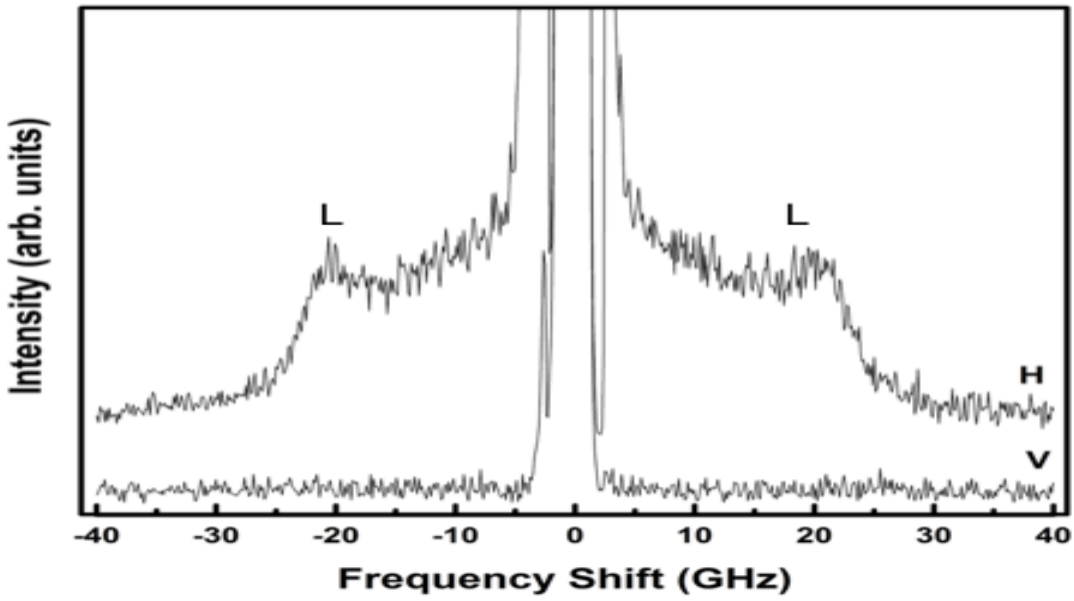

Figure 4.18: Brillouin spectra of Sb_2Te_3-1. V: vertically-polarized scattered light, H: horizontally-polarized scattered light (H). The incident light was horizontally polarized in both cases.

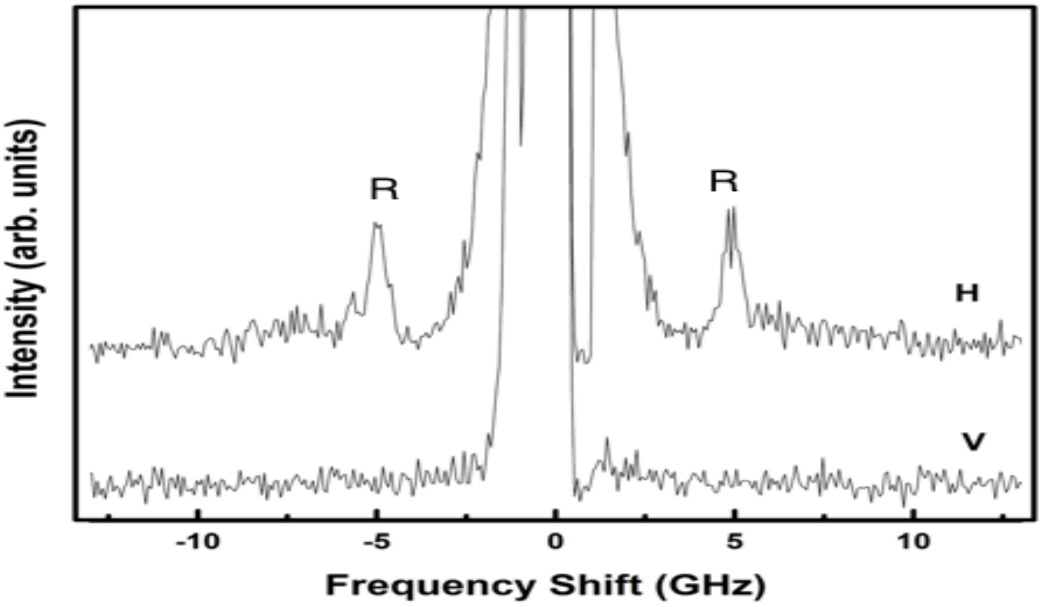

Figure 4.19: Brillouin spectra of Sb_2Te_3-2. V: vertically-polarized scattered light, H: horizontally-polarized scattered light (H). The incident light was horizontally polarized in both cases.

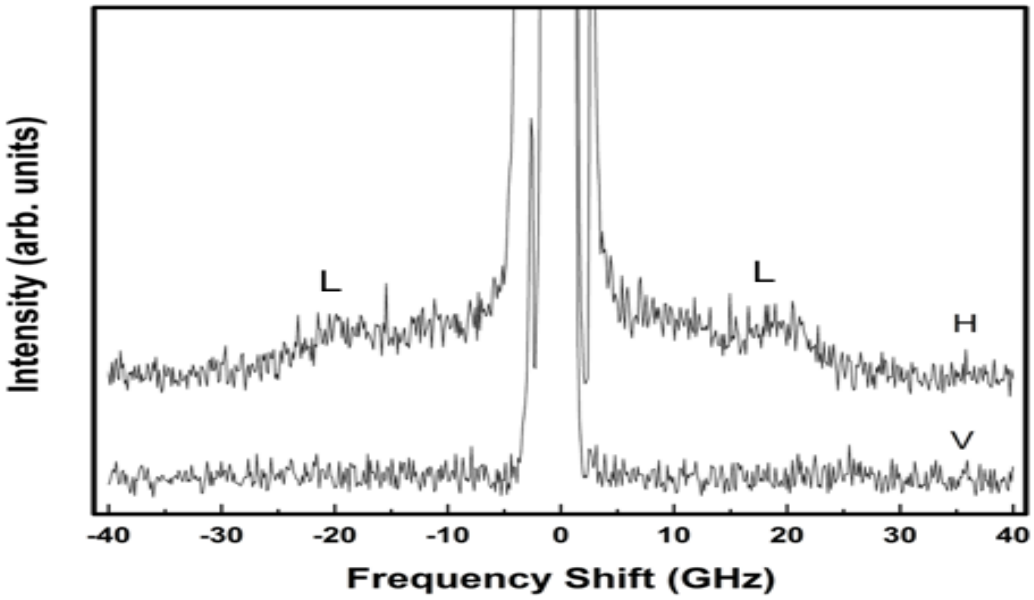

Figure 4.20: Brillouin spectra of Sb_2Te_3-2. V: vertically-polarized scattered light, H: horizontally-polarized scattered light (H). The incident light was horizontally polarized in both cases.

Table 4.6: Velocities of Rayleigh and longitudinal bulk modes of Sb_2Te_3-1 and Sb_2Te_3-2.

Sample	v_R ($\pm 100\ m/s$)	v_L ($\pm 80\ m/s$)
1	1420	3340
2	1500	3350
Average	1500	3300

The Rayleigh surface and longitudinal bulk phonon velocities of the two samples of Sb_2Te_3 studied are given in Table 4.6. There is good agreement between both the Rayleigh surface phonon and longitudinal bulk phonon velocities for both samples. Using Equation (2.10), the elastic constant C_{33} was found to be 72 ±3 GPa.

4.4 Bismuth Telluride (Bi_2Te_3)

Figures 4.21 and4.22 show spectra collected from Bi_2Te_3-1 and Bi_2Te_3-2, respectively, at angles of incidence from 40^o to 70^o with the FSR set to 15 GHz. One set of Brillouin peaks was observed at lower frequency shift which is labelled R. The R peak was seen for all angles of incidence for the second sample. However, even though attempts were going on for days to see this peak at different angles, it was seen only at 40^o for the first sample for unknown reasons, and was extremely weak for both samples (see Figure 4.22). It can be seen that the frequency shift of R peak increases with increasing angle of incidence. Once the data of R peak was obtained, the free spectral range was increased to 50 GHz to see Brillouin peaks at higher frequency shifts. Figures 4.23 and 4.24 show spectra collected from Bi_2Te_3-1 and Bi_2Te_3-2, respectively, at various angles from 40^o to 70^o with the FSR set to 50 GHz. Two sets of Brillouin peaks were observed and are labelled T_1 (since only one quasi-transverse bulk mode was observed and shows excellent agreement with literature as shown in Table 4.9) and L. Since the range of angles used here was $40^o - 70^o$, the range of directions probed inside the material was found by Snell's law to be 8^o. That is, the bulk phonons that were probed travelled in directions from 16^o to 24^o from the z-axis. Accordingly, the change in the frequency shifts of the these peaks with angle of incidence is small.

Table 4.7 presents the average frequency shifts of the R, T_1, and L peaks for different angles of incidence for Bi_2Te_3-1 and Bi_2Te_3-2.

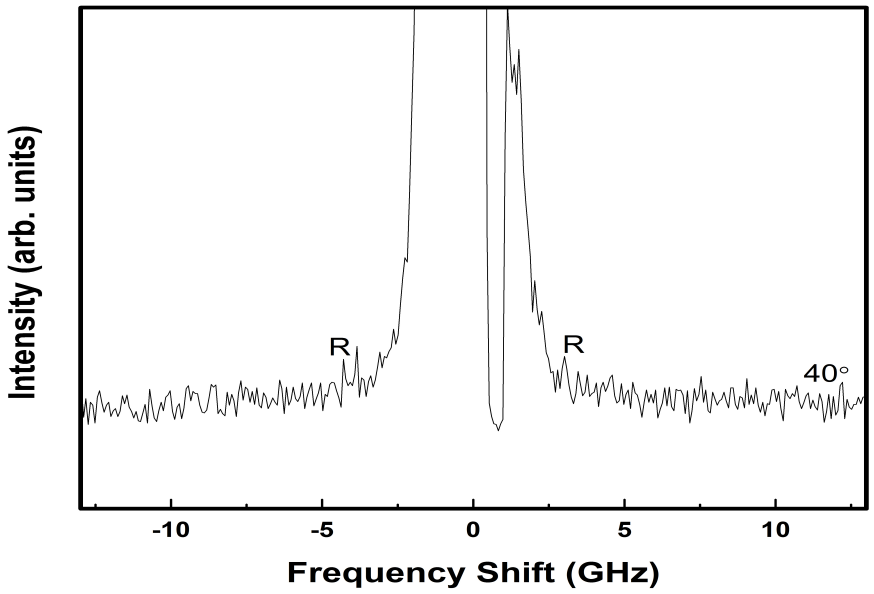

Figure 4.21: Billouin spectra of Bi_2Te_3-1 collected at 40^o of incidence. The free spectral range was set to 15 GHz.

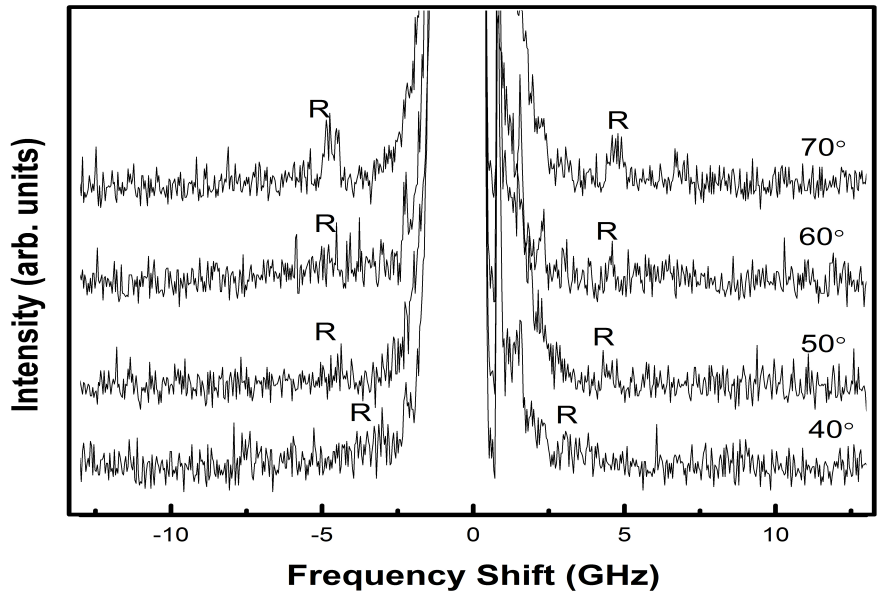

Figure 4.22: Billouin spectra of Bi_2Te_3-2 collected at various angles of incidence. The free spectral range was set to 15 GHz.

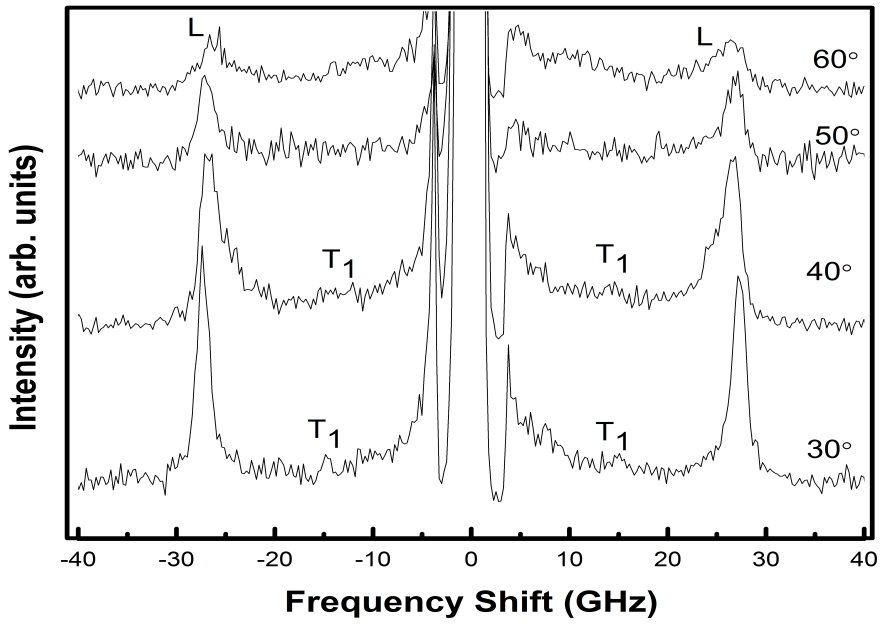

Figure 4.23: Billouin spectra of Bi_2Te_3-1 collected at various angles of incidence. The free spectral range was set to 50 GHz.

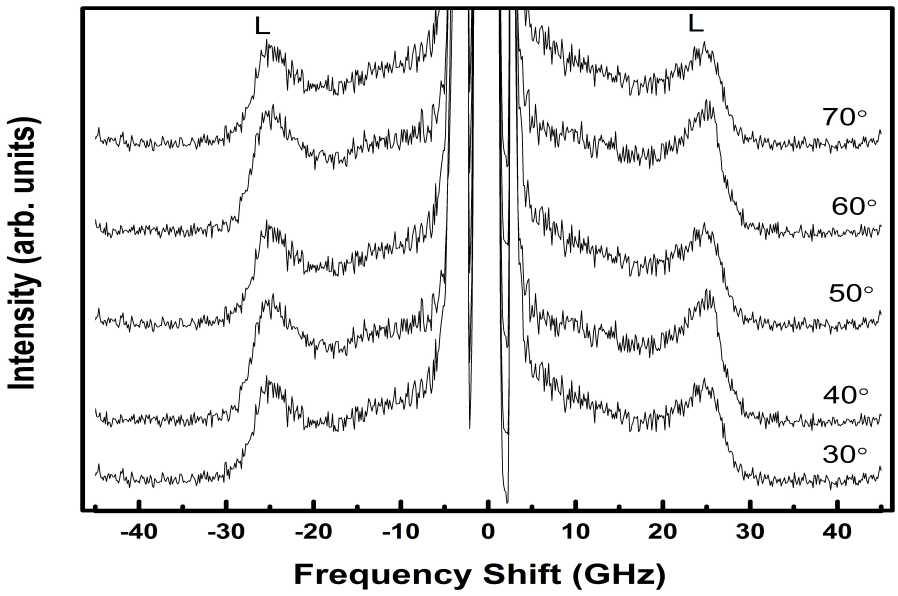

Figure 4.24: Billouin spectra of Bi_2Te_3-2 collected at various angles of incidence. The free spectral range was set to 50 GHz.

From Figures 4.23 and 4.24 two different peaks are distinguished: one is labelled L which appears at higher frequency shift and T_1 which is seen at low frequency shifts in the Brillouin scattering spectrum.

Frequency shift data for samples Bi_2Te_3-1 and Bi_2Te_3-2 is given in Table 4.7. As can be seen, the frequency shifts of the T_1 and L peaks vary little with angle of incidence due to the small range of directions probed inside the material. The frequency shift of the R peak, however, increases with increasing angle of incidence.

Using the data in Table 4.7, the frequency shift of R peak for $Bi_2Te_3$3 -2 is plotted against sine of the angle of incidence as shown in Figure 4.26. It can be seen that the shift of this peak depends linearly on sine of the angle of incidence. Equation (2.21) fitted well to this data and confirmed that the R peak is due to the Rayleigh surface mode. As for $Bi_2Se_3$3 and $Sb_2Te_3$3, the velocity of this mode, v_R, was extracted from

Table 4.7: The avarage frequency shifts of all peaks observed from Bi_2Te_3-1 and Bi_2Te_3-2

Sample	Angle of incidence ($\pm 1^o$)	f_R Shift ($\pm$0.3 GHz)	f_{T1} Shift ($\pm$0.3 GHz)	f_L Shift ($\pm$0.2 GHz)
1	30	-	16.3	26.4
	40	3.5	16.4	26.2
	50	-	-	26.4
	60	-	-	26.3
2	30	3.9	-	24.6
	40	4.4	-	24.4
	50	4.6	-	24.7
	60	5.7	-	24.4

the slope of the line of best fit and as given in Table 4.8.

The relative independence of the frequency shifts of the T_1 and L peaks on angle of incidence suggests that they are due to bulk quasi-transverse and quasi-longitudinal acoustic modes, respectively. As can be seen in Figure 4.28, there is asymmetry in the shape of the L peak: there is shoulder on the low frequency shift side. This asymmetry may be due to transverse modes around 15 GHz. Such partial overlap causes the peaks to be artificially-shifted toward each other. The effect of the overlap can be seen in Figures 4.24 and 4.28 which show spectra collected with no polarization analysis of the scattered light and with a polarizer in the scattered light. In the former case, the frequency shift of the L peak is 26 GHz while in the latter it is 24 GHz for HH polarization (in which case contributions to the appearance from T modes should be reduced).

As shown in Figures 4.28 and 4.27, the L peak remains with horizontal polarization (HH) and disappeared with vertical polarization (HV). This suggest that this peak is due to a bulk quasi-longitudinal mode. Using Equation (2.32) along with the average frequency shift in Table 4.7 and the refractive index value presented in Table 3.1, the velocities of these modes, v_{T1} and v_L, were determined and given in Table 4.8.

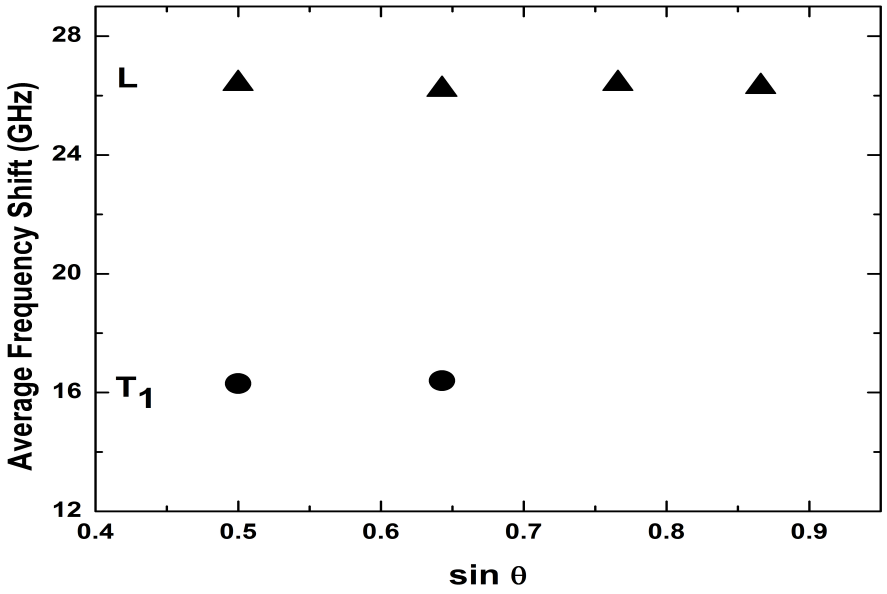

Figure 4.25: Average frequency shifts of Brillouin peaks versus sine of the angle of incidence for sample Bi_2Te_3-1. δ^o=±1^o, δT_1= ±0.3 GHz, and δL= ±0.2 GHz.

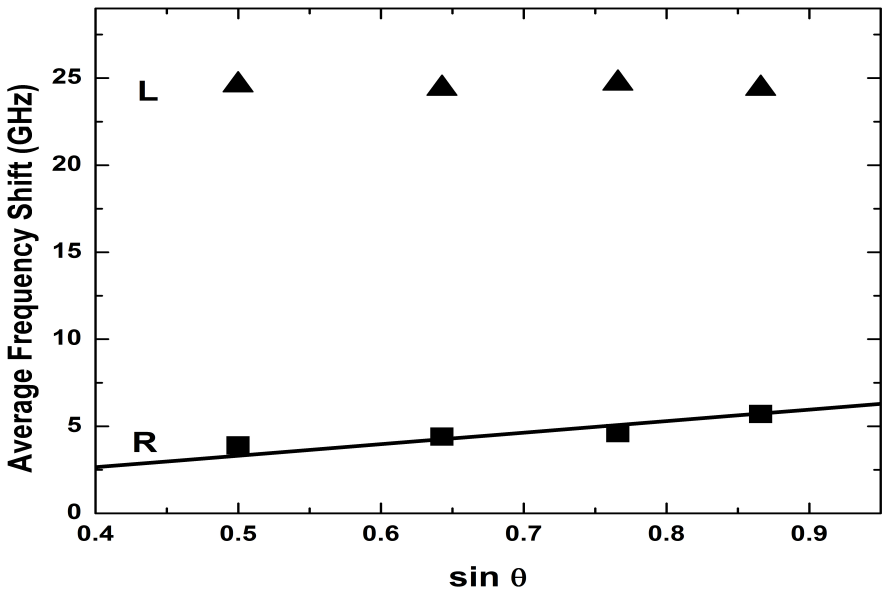

Figure 4.26: Average frequency shifts of Brillouin peaks versus sine of the angle of incidence for sample Bi_2Te_3-2. δ^o=±1^o, δR= ±0.3 GHz, and δL= ±0.2 GHz, R^2= 0.977.

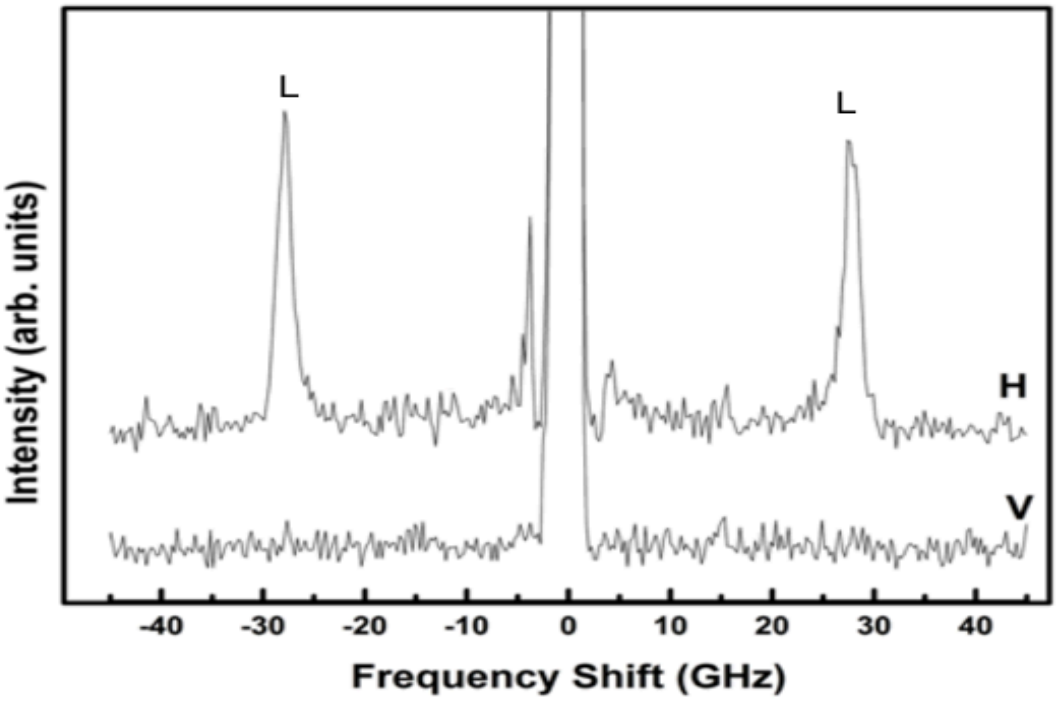

Figure 4.27: Brillouin spectra of Bi_2Te_3-2. V: vertically-polarized scattered light, H: horizontally-polarized scattered light (H). The incident light was horizontally polarized in both cases.

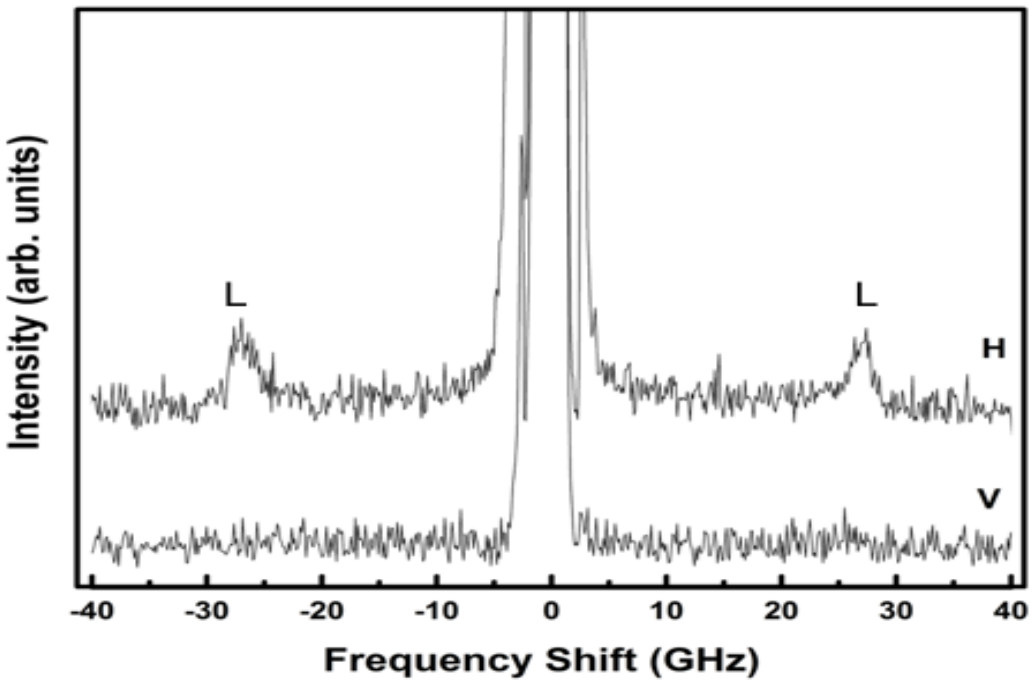

Figure 4.28: Brillouin spectra of Bi_2Te_3-2. V: vertically-polarized scattered light, H: horizontally-polarized scattered light (H). The incident light was horizontally polarized in both cases.

Table 4.8: Phonon velocities of Bi_2Te_3-1 and Bi_2Te_3-2

Sample	v_R ($\pm 100\ m/s$)	v_{T1} ($\pm 100\ m/s$)	v_L ($\pm 125\ m/s$)
1	-	1800	2670
2	1400	-	2550
Average	-	-	2600

Using Equations 2.10 and 2.11, and knowing the density, quasi-longitudinal and quasi-transverse phonon velocities, elastic constants C_{33} and C_{44} have been estimated to be 52 ±5 GPa and 25 ±2 GPa, respectively.

4.5 Discussion

From Table 4.9, it is clearly seen that the Rayleigh surface phonon velocity for all these materials is similar. This is not surprising since Bi_2Se_3, Sb_2Te_3, and Bi_2Te_3 belong to the same family of topological insulators and have similar properties. By comparing the longitudinal bulk phonon velocities for Bi_2Se_3 and Sb_2Te_3, it can be seen that their velocities are similar differing only by 9% (the difference between the two values was divided by the average of them and multiplied by 100 to obtain the difference percentage) . However, a remarkable difference (30%) is seen when comparing the longitudinal bulk phonon velocity of Bi_2Te_3 to the other two materials. Similarity is seen between the slow transverse phonon velocity of Bi_2Te_3 and Bi_2Se_3, and the difference is just about 8%.

Table 4.9: Acoustic phonon velocities of Bi_2Se_3, Sb_2Te_3, and Bi_2Te_3 determined from this work and compared to other's findings. Experimental results are denoted by Exp. All others are theoretical.

Material	Reference	v_R (m/s)	T_1 (m/s)	T_2 (m/s)	L (m/s)
Bi_2Se_3	Present	1400 ±100	2000 ±80	2500 ±140	3800 ±170
Sb_2Te_3	Present	1500 ±100	-	-	3300 ±170
	[10]	-	-	2230	3840
Bi_2Te_3	Present	1400 ±100	1800 ±80	-	2600 ±170
	[17]	-	1780	-	3040
	[10]	-	1390	2170	2880
	[18]	-	1800 ±50	-	2400 ±50
$Bi_{1.60}Sb_{.40}Te_3$	[19] Exp	-	1870	-	2380

Table 4.10 presents elastic constants of Bi_2Se_3, Sb_2Te_3, and Bi_2Te_3, and compares some of these results to other studies where the methods used were not Brillouin Scattering.

Table 4.10: Elastic constants (in GPa) of Bi_2Se_3, Sb_2Te_3, Bi_2Te_3, and $Bi_{1.60}Sb_{0.40}Te_3$. Experimental results are denoted by Exp. All others were determined from theory.

Material	Reference	C_{11}	C_{12}	C_{13}	C_{66}	C_{33}	C_{44}
Bi_2Se_3	Present work	-	-	-	-	98 ±7	37 ±10
	[16]	110.9	38.4	48.1	35.9	96.1	62.2
Bi_2Te_3	Present work	-	-	-	-	52 ±5	25 ±2
	[12] Exp	68.4	21.7	27	23.3	47.6	27.3
	[14]	62	10	19	22.5	49	24
	[12] 80K	73.3	21.9	28.7	25.7	50.8	30.5
	[13]	88.33	18.23	29.32	23.8	53.31	37.70
	[10]	73.8	16.3	30.6	28.7	54.3	30.4
	[11]	82.8	20.8	36.1	31	60.4	40.1
	[15]	65.4	10.9	19	25.7	50.7	26.5
Sb_2Te_3	Present work	-	-	-	-	72 ±3	-
	[10]	83.2	21.2	46.1	31	99.7	44.6
$Bi_{1.60}Sb_{0.40}Te_3$	[19] Exp	66.6	12.6	33.0	27.0	44.0	27.1
	[19] 77K Exp	72.2	12.9	35.3	29.6	47.9	29.7

As shown in Table 4.9 acoustic phonon velocities of Bi_2Se_3, Sb_2Te_3, and Bi_2Te_3 have different values. It was not possible to find all acoustic velocities for all materials in this work, nor other studies were able to obtain all of them. The Rayleigh surface phonon velocity of the three materials were not found in other studies. Using the bulk phonon velocities in this table, the values of the elastic constants of our materials have been determined and illustrated in Table 4.10. A brief discussion about the acoustic phonon velocities and the elastic constants for each material is presented below.

4.5.1 Bismuth Selenide (Bi_2Se_3)

The Rayleigh surface phonon velocity (v_R) has been calculated and found to be 1400±100 m/s. Table 4.9 also shows the values of slow and fast transverse (T_1 and T_2) and longitudinal (L) acoustic phonon velocities. There are no other studies that report acoustic phonon velocities for Bi_2Se_3. These velocity values were used to calculate elastic constants C_{33} and C_{44} as mentioned in section (4.2). The values of C_{33} and C_{44} were found by us to be 98 and 37 GPa, respectively. By comparison with the theoretical calculated values as provided by reference [16], excellent agreement is observed between the C_{33} experimentally obtained and theoretically calculated values. However, a remarkable difference (roughly 38%) is observed for C_{44}. Such a difference indicates that the model used in this theoretical study [16] does not accurately predict the elastic properties of this material. It is worth noting, however, that our value for C_{44} for Bi_2Te_3 is consistent with that found in other studies on this material [15, 12]. This produces some support for the accuracy of our value of C_{44} for Bi_2Se_3.

4.5.2 Bismuth Telluride (Bi_2Te_3)

In a similar manner to that of Bi_2Se_3, the surface phonon velocity (v_R) has been found to be 1400±100 m/s. It was not possible to compare this number with other studies due to the absence of related theoretical and experimental studies on this material. It was, however, possible to compare our values of transverse and longitudinal acoustic phonon velocities to those obtained in other studies [10, 17, 18]. The transverse phonon velocity T_1 of Bi_2Te_3 was theoretically reported in [17] and [18] and experimentally in reference [19], and excellent agreement is observed between the velocity obtained in this work and these studies. The values presented in references [17] (i.e 1780 m/s) and [18] (i.e, 1800 m/s) are very similar to the value obtained by

us (i.e. 1800±100) m/s. These two theoretical studies have been also experimentally confirmed as shown in reference [19] (i.e. 1870 m/s), along with the value found in our work. However, the value shown in reference [10] (i.e. 1390 m/s) is substantially different from the theoretical and experimental values mentioned above. This may suggest that the model used in reference [10] is not accurate for such investigations. The longitudinal bulk phonon velocity (L) of the present work was calculated to be 2600 ±170 m/s and is, in general, in good agreement with the theoretical studies as in references [10, 17, 18].

In regard to the elastic constant calculations, our experimental data have been found to be in excellent agreement with other experimental findings shown by references [12] and [19]. It is also interesting to note that our values of C_{44} for Bi_2Te_3 (i.e, 25 GPa) is nearly identical to the value found in the theoretical study of reference [14]. Our value of C_{33} and C_{44} are similar to those values obtained in several other theoretical studies. For instance, the values of the elastic constants observed in the studies conducted in references [15] (i.e, C_{33}=50.7 GPa and C_{44}=26.5 GPa) and [19] (i.e, C_{33}=44.0 GPa and C_{44}=27.1 GPa) have been found very close to those obtained here (i.e, C_{33}=52 GPa and C_{44}=25 GPa). However, such close agreement with other theoretical results was not always observed. This can be seen in the result found by reference [11], in which the value of C_{44} was greatly different (roughly 40%) than that found in this work. It is worth noting that the value of C_{33} and C_{44} obtained in reference [19] are very similar to those for Bi_2Te_3 obtained in this work (roughly 8%). This may be due to that Bi_2Te_3 is very close in composition to $Bi_{1.60}Sb_{0.40}Te_3$, and therefore very similar in elastic properties. Based on the aforementioned discussion, it can be stated that the inconsistency in the theoretical results may make the comparison between theoretical and experimental results invalidate some of the theoretical values used to calculate the elastic properties.

4.5.3 Antimony Telluride (Sb_2Te_3)

Similar to the previous two situations, v_R of Bi_2Te_3 has been calculated (i.e,1500 ±100 m/s) but there are no other studies which present these velocities for comparison. However, it is worthwhile to note that the v_R of all three materials studied in this work are very close to each other. Moreover, comparing the quasi-longitudinal phonon velocity obtained in the present work (i.e. 3300±170 m/s) to the only available obtained data in literature [10], good agreement (roughly 15%) is observed which supports this study.

Table 4.10 shows the elastic constants of Sb_2Te_3. The value of the elastic constant C_{33} of Sb_2Te_3 was experimentally determined in the present study and found to be 72 GPa. This elastic constant could only be compared with a theoretical value since only theoretical results have been considered in the literature [10]. Our experimentally obtained value was found to be different from the theoretically calculated value in reference [10] (roughly 30%). However, there has been one study on $Bi_{1.60}Sb_{0.40}Te_3$ [19]. Taking into the account the claim made in this reference [19] that the effect of the mixture between the elements Bi, Sb and Te can be negligible, the C_{33} value for Sb_2Te_3 should have a similar value to that of $Bi_{1.60}Sb_{0.40}Te_3$. However, a remarkable difference is seen which concludes that such mixture has an effect on the determination of the elastic constants of this material. It is worth noting that the value of C_{33} obtained in reference [19] is different (roughly 13%) from the value obtained in this work (see Table 4.10). This may be due to that Sb_2Te_3 is not close in composition to $Bi_{1.60}Sb_{0.40}Te_3$, and therefore not close in elastic properties.

It is lastly important to state that excellent agreement between our values and the values observed by others with different experimental techniques such as continuous wave resonance [12] and ultrasonic pulse-echo [19] obviously indicate that Brilliuoun Scattering technique is capable of providing precise results for the investigation of the elastic constants of this family of topological insulators.

Chapter 5

Conclusions

Brillouin light scattering has been used to investigate three different Topological Insulators: Bismuth Selenide Bi_2Se_3, Antimony Telluride Sb_2Te_3, and Bismuth Telluride Bi_2Te_3. Three different results of acoustic waves were obtained : surface mode, quasi-longitudinal, and quasi-transverse bulk modes. The longitudinal bulk phonons as well as surface phonons were seen for all these topological insulators. However, the transverse bulk mode was observed only for Bi_2Se_3 and Bi_2Te_3. All acoustic modes obtained from this work were verified by polarization studies. From Brillouin frequency shifts, it was possible to calculate longitudinal , transverse bulk and surface phonon velocities. In general, comparing the obtained acoustic phonon velocities of these materials in this work has been found to be in excellent agreement with the available data. From acoustic phonon velocities obtained from Brillouin frequency shifts, C_{33} and C_{44} have been calculated. Excellent agreement is obtained between our findings for Bi_2Te_3 elastic constants with some theoretical and experimental studies available [15, 12, 19], while our values disagree with others [11]. Our result for C_{33} is consistent with the calculated value in reference [16] for Bi_2Se_3, while C_{44} is not. Finally, a remarkable difference was seen between the C_{33} value of Sb_2Te_3 obtained

in the present work and the value calculated in reference [10] .

Possible future work could involve Brillouin studies using a different scattering geometry or crystal orientation. This would permit the remaining four elastic constants of these materials to be determined. Since phonons propagate away from the z-axis by more a few degrees in such geometry, both transverse modes would be seen, and that might allow calculation of additional elastic constants.

Bibliography

[1] M. Zuo, D. Ling, and L. Sheng. Phys. Lett. A. **377**, 2909 (2013).

[2] H. Li, J. Shao, and H. Zhang. Nanoscale. **6**, 3127 (2013).

[3] Y. Liu, Z. Ma, and Y. Zhao. Chin. Phys. B. **22**, 067302 (2013).

[4] E. Joel. Nature. **464**, 194 (2010).

[5] R. J. Cava, W. Ji, and M. Fuccillo. J. Mater. Chem. **1**, 3176 (2013).

[6] L. Fu. Phys. Rev. Lett. **106**, 106802 (2010).

[7] M. Hasan and C. Kane. Rev. Mod. Phys. **82**, 3045 (2010).

[8] C. X. Lio, X. L. Qi, and H. Zhang. Phys. Rev. **82**, 045122 (2010).

[9] E. Hatta and K. Mukasa. J. Appl. Phys. **105**, 4807 (1998).

[10] H. Koc, A. Mamedov, and E. Ozbay. IEEE International Symposium. p. 41 (2014).

[11] Z. Xiong, X. An, Z. Li, T. Xiao, and X. Chen. J. Alloys Compd. **586**, 392 (2014).

[12] J. O. Jenkins and J. A. Rayne. Phys. Rev. B. **5**, 3171 (1972).

[13] S. Feng and S. Li. Comput. Mater. Sci. **82**, 45 (2014).

[14] Y. Tong, F. Yi, L. Liu, and P. Zhai. Comput. Mater. Sci. **48**, 343 (2010).

[15] B. Huang and M. Kaviany. Phys. Rev. B **77**, 125209 (2008).

[16] H. koc, Ozisik, E. Deligoz, H. Mamedov, H. Ozisik, E. Deligoz, M. Amirullah, Mamedov, and E. Ozbay. J Mol Model. **20** (2014).

[17] F. Yang, T. Lkeda, G. Snyder, and C. Dames. J. Appl. Phys. **108**, 034310 (2010).

[18] A. Jacqout, M. Bayer, H. Winkler, and M. Jeagle. J. Solid State Chem. **193**, 105 (2012).

[19] Y. C. Akgoz, G. A. Saunders, and Z. Sumengen. J. Mater. Sci. **7**, 2979 (1972).

[20] W. Burr. The elasticity and resistance of the materials of engineering (John Wiley and Sons 1988).

[21] L. Landau and E. Lifshitz. *Theory of Elasticity* (Pergamon Press 1970).

[22] H. Ibach. *Solid-State Physics: An Introduction to Principles of Materials Science*, (Springer, New York2009), 4th ed.

[23] J. Nye. *Physical Properties of Crystals* (Clarendon Press 1985).

[24] M. Musgrave. *Crystal Acoustics* (Holden-Day 1970).

[25] D.Sirdeshmukh, L. Sirdeshmukh, and K. Subhadra. *Micro-and Macro- Properties of Solids* (Springer Series in Material Science 2006).

[26] E. Gross. Nature. **126**, 211 (1930).

[27] E. S. Zouboulis, M. Grimsditch, A. K. Ramdas, and S. Rodriguez. Phys. Rev. B. **57**, 2889 (1988).

[28] M. Tateda, T. Horiguchi, Kurashima, and K. T. Ishihara. J. Lightwave Technol. **8**, 1269 (1990).

[29] L. C. Parsons and G. T. Andrews. Appl. Phys. Lett. **95**, 123521 (2009).

[30] S. F. Ahmed, H. Kiefte, M. J. Clouter, and M. D. Whitmore. Phys. Rev. B. **26**, 4239 (1982).

[31] J. Ferraro and K. Nakamoto. *Raman Spectroscopy* (Elsevier Science 2003).

[32] S.-L. Zhang. *Raman Spectroscopy and its Application in Nanostructures*, (John Wiley and sons2012).

[33] H. Kuzmany. *Solid-State Spectroscopy: An Introduction*, (Springer, New York2009), 2nd ed.

[34] J. R. Sandercock. Solid St. Commun. **26**, 547 (1978).

[35] V. Bortolani, F. Nizzoli, G. Santoro, A. Marvin, and J. R. Sandercock. Phys Rev. Lett. **43**, 224 (1979).

[36] W. Weber and R. Merlin. Raman scattering in materials science (Berlin: Springer-verlag Berlin Heidelgerg 2000).

[37] W. Hayes and R. Loudon. *Scattering of Light by Crystals* (Dover Publications 2004).

[38] W. Zhang, R. Yu, and H. Zhang. New J. Phys. **12**, 065013 (2010).

[39] M. Marder. Condensed matter physics (John Wiley and Sons 2010).

[40] J. R. Sandercock. IEEE **18** (1982).

[41] C. Kittel. Introduction to solid state physics (John Wiley and Sons 1971).

[42] Y. L. Chen, J. Chu, G. Analytis, Z. K. Liu, K. Igarashi, H. Kuo, X. L. Qi, S. K. Mo, R. G. Moore, D. H. Lu, M. Hashimoto, T. Sasagawa, S. C. Zhang, I. R. Fisher, Z. Hussain, and Z. X. Shen. Science. **329**, 659 (2010).

[43] Operation and service manual. *Maxtek Film Deposition Controller*. Cypress (2005).

[44] S. advanced material. Material safety sheet of sb_2te_3. Irvine. USA (2012).

[45] S. advanced material. Material safety sheet of bi_2te_3. Irvine. USA (2012).

[46] J. Zhang, Z. Peng, A. Soni, and V. Zhao. Nano.Lett. **6**, 2407 (2011).

[47] M. Meuberger. *The Bismuth Telluride – the Bismuth Selenide System* (1966).

[48] H. Cui and L. a. Bhat. J. Electron. Mater. **28**, 10 (1999).

[49] M. Kuwahara, R. Endo, and K. Morikasa. Appl. Phys. Lett. **10**, 101910 (2012).

[50] C. Hamaguchi. Basic semiconductor physics (Springer 2001).

[51] R. Wolfe. Introduction to imaging spectrometers (SPIE- the international society for optical engineering 1997).

[52] J. Vaughan. The fabry-perot interferometer history, practice and applications (Taylor and Francis group 1989).

[53] A. Dutta, N. Dutta, and M. Fujiwara. Wdm technologies: Passive optical components: Passive optical components (Elsevier science 2003).

[54] G. Laufer. Introduction to optics and lasers in engineering (Cambridge University Press 1996).

[55] K. Iizuka. Elements of photonics in free space and special media (John Wiley and Sons 2002).

[56] K. Ulrich, Renk, and L. Genzel. IEEE Trans. Microw. Theory Tech. **11**, 363 (1963).

[57] J. R. Sandercock. *Tandem Fabry-Perot Interferometer TFP-1 Operator Manual*. JRS Scientific Instruments (2001).

[58] C. Wang, X. Zhu, L. Nilsson, J. Wen, G. Wang, X. Shan, Q. Zhang, S. Zhang, J. Jia, and X. Q. Nano Res. **9**, 688 (2013).